

Molecular gas budget of strongly magnified low-mass star-forming galaxies at cosmic noon

V. Catán¹, J. González-López^{1,2}, M. Solimano³, L. F. Barrientos¹, A. Afruni⁴, M. Aravena³, M. Bayliss⁵, J. A. Hernández¹, C. Ledoux⁶, G. Mahler^{7,8,9}, and N. Tejos¹⁰

¹ Instituto de Astrofísica, Facultad de Física, Pontificia Universidad Católica de Chile, Av. Vicuña Mackenna 4860, 782-0436 Macul, Santiago, Chile

e-mail: victoria.catan@uc.cl

² Las Campanas Observatory, Carnegie Institution of Washington, Raúl Bitrán 1200, La Serena, Chile

³ Núcleo de Astronomía de la Facultad de Ingeniería y Ciencias, Universidad Diego Portales, Av. Ejército Libertador 441, Santiago, Chile

⁴ Kapteyn Astronomical Institute, University of Groningen, Landleven 12, 9747 AD Groningen, The Netherlands.

⁵ Department of Physics, University of Cincinnati, Cincinnati, OH 45221, USA

⁶ European Southern Observatory, Alonso de Córdova 3107, Vitacura, Casilla 19001, Santiago, Chile

⁷ STAR Institute, Quartier Agora - Allée du six Août, 19c B-4000 Liège, Belgium

⁸ Centre for Extragalactic Astronomy, Durham University, South Road, Durham DH1 3LE, UK

⁹ Institute for Computational Cosmology, Durham University, South Road, Durham DH1 3LE, UK

¹⁰ Instituto de Física, Pontificia Universidad Católica de Valparaíso, Casilla 4059, Valparaíso, Chile

August 16, 2024

ABSTRACT

Aims. This study aims to investigate the molecular gas content of strongly magnified low-mass star-forming galaxies around the cosmic noon period ($z \sim 2$) through observations of CO emission lines and dust continuum emission, both of which serve as tracers for molecular gas.

Methods. We observed twelve strongly lensed galaxies with the Atacama Compact Array to detect CO mid-j rotational transitions and dust continuum. Thanks to the strong lensing, we were able to probe the low-mass regime, previously understudied. With a compiled set of observations, we recalibrate empirical relations between star formation rate density and the CO line ratios. Using Spectral Energy Distribution fitting, we derived galaxy properties, and we also performed galaxy stacking to combine the faint signals. In all cases, molecular gas masses were estimated using both tracers.

Results. We detected CO emission in three out of 12 galaxies and dust continuum emission in three of them. The obtained molecular gas masses indicate that most of these galaxies ($M_* < 10^{10.7} M_\odot$) have lower molecular gas fractions and shorter depletion times compared to the expectations from established scaling relations at these redshifts. Several possible explanations for this gas deficit were explored, including uncertainties in mass estimates, effects of low metallicity environments, larger atomic gas reservoirs in low-mass systems, and the possibility that these represent low-mass analogs of "main sequence starburst" galaxies, which are undergoing sustained star formation due to gas compaction despite low overall gas fractions.

Conclusions. We conclude that there is a molecular gas deficit at these mass and metallicity regimes. Our results suggest that this deficit is likely due to a significant amount of atomic gas, which our stacking indicates is about 91% of the total gas. However, this estimation might be an upper limit in the case of our galaxies containing CO-dark gas.

Key words. Star forming galaxies – gravitational lensing – galaxy evolution – molecular gas – CO emission

1. Introduction

Star formation represents a fundamental astrophysical process mainly occurring within dense, cold molecular clouds. Examining this gas at high redshifts provides insight into galaxy assembly and evolution since it is the primary fuel for star formation (Carilli & Walter, 2013; Tacconi et al., 2020). The cosmic noon period, characterized by a pronounced peak in the cosmic star formation rate density around $z \sim 2$ (e.g., Madau & Dickinson, 2014), is a key epoch to study the molecular gas (H_2) content of galaxies. However, studying H_2 poses a significant challenge at this time, primarily due to the complexities associated with its detection. Consequently, being able to study H_2 during this period holds promise for advancing our understanding of galaxy evolution.

Directly observing H_2 , the most abundant molecule at high redshift, poses a significant challenge due to its high excitation requirements, even for the lowest transitions (Carilli & Walter, 2013; Saintonge & Catinella, 2022). As a result, astronomers have historically relied on proxies, such as carbon monoxide (CO) for its study (Carilli & Walter, 2013; Tacconi et al., 2020; Saintonge & Catinella, 2022). There is a preference for this proxy which arises from its abundance and relatively low excitation requirements, which are facilitated by collisions with H_2 molecules (Carilli & Walter, 2013).

The use of CO as a tracer requires the use of a conversion factor, α_{CO} (Carilli & Walter, 2013; Tacconi et al., 2020; Saintonge & Catinella, 2022), defined by Equation 1.

$$M_{\text{mol}} = \alpha_{CO} L'_{\text{CO}(1-0)} \quad (1)$$

This factor has been seen to vary with metallicity, although the exact relationship remains incompletely constrained. Consequently, several models have been developed to estimate α_{CO} . Some of these models (Wilson, 1995; Magdis et al., 2011; Genzel et al., 2012; Schruba et al., 2012; Genzel et al., 2015; Accurso et al., 2017; Tacconi et al., 2018; Madden et al., 2020) are compared in Fig. 6. Most models indicate general agreement near solar metallicities but show discrepancies at higher or lower metallicity values. They are also all inversely proportional as CO gets photo dissociated at low metallicities (Tacconi et al., 2020).

From the study of CO observations, several authors have established redshift-dependent scaling relations between the molecular gas content and galaxy properties (Dessauges-Zavadsky et al., 2015; Tacconi et al., 2018; Aravena et al., 2019; Tacconi et al., 2020). Such studies indicate a decreased molecular gas depletion timescale and increased molecular gas fraction with increasing redshift. It’s important to note that at high redshift, most studies focus on high-mass galaxies, leaving a gap in our understanding of their low-mass counterparts. As a result, there is a significant lack of research on the molecular gas budget in high redshift low-mass galaxies, which calls for dedicated research to address this gap.

Gravitational lensing has emerged as an invaluable tool for addressing this deficit, as it facilitates the detection of low-mass galaxies at high redshifts. Strong Gravitational lensing by groups or clusters of galaxies can act as “cosmic telescopes”, magnifying the light from faint background galaxies. The magnification effect makes sources appear larger in the sky while preserving their surface brightness, thus allowing us to observe faint galaxies at high redshift, which usually appear as gravitational arcs (e.g., Sharon et al., 2020, 2022c). Previous works such as Dessauges-Zavadsky et al. (2015) and Saintonge et al. (2013) have studied high redshift lensed galaxies and obtained their molecular gas contents. These studies, which used CO tracers, focused on star-forming galaxies (SFGs) and found lower depletion times and similar gas fractions as $z \sim 1$ main sequence (MS) galaxies. Similarly, Solimano et al. (2021) analyzed four strongly lensed, low-mass galaxies at $z \sim 2$ and found relatively low depletion times and gas fractions, which indicated a possible molecular gas deficit in low-mass galaxies.

Building upon the groundwork laid by Solimano et al. (2021), our present study aims to deepen the understanding of the apparent gas deficit they found. Our approach involves measuring the CO emission lines of 12 gravitationally lensed galaxies with literature-reported stellar masses below $10^{10.5} M_{\odot}$ as Solimano et al. (2021) found that they might have different gas reservoirs to their high-mass counterparts. The redshifts studied span from 1.91 to 3.625, thus belonging to the cosmic noon period. The galaxies are part of the Sloan Digital Sky Survey Giant Arcs Survey (SGAS) (Hennawi et al., 2008), making them all strongly magnified sources. To enhance the reliability of our findings, we will implement new methodologies for estimating the luminosity conversion ratios and use the method presented in Tsukui et al. (2023) to estimate interferometric errors. We also explored how stacking these galaxies provided information about the average galaxy at these redshifts.

The paper is organized as follows: In Sect. 2, we present the sample, the ACA observations, and the ancillary data. In Sect. 3, we present our methods and main results. In Sect. 4, we discuss and interpret the results. Finally, we report our main conclusions in Sect. 5.

For this study, we employed a flat Λ CDM cosmology, adhering to the following parameter values: energy density parameter (Ω_{Λ}) = 0.7, and matter density parameter (Ω_M) = 0.3. All

flux densities were expressed relative to frequency (f_{ν}), ensuring consistency and accurate comparisons across observations. Additionally, we adopted the initial mass function (IMF) derived by Chabrier (2003).

2. Observations

2.1. Sample selection

The sample analyzed in this paper comprises 12 SGAS galaxies (Hennawi et al., 2008), four previously studied by Solimano et al. (2021), and eight additional galaxies selected to expand their study. The primary selection criterion was stellar mass, as we aimed to investigate the molecular gas content of low-mass galaxies. Consequently, all galaxies in the sample have literature reported stellar masses below $10^{10.5} M_{\odot}$. More details about the galaxies are reported in Table 1. For the galaxies’ metallicities, we used the STARBURST99 (SB99) (Leitherer et al., 1999) values obtained from Chisholm et al. (2019) and Bayliss et al. (2014), following the procedure outlined by Solimano et al. (2021). For sources without previous metallicity measurements, we assumed a mass-metallicity relation from Sanders et al. (2021) to estimate them. As their masses and redshifts apply to our sample. From this, we can see that the galaxies are also characterized by their low metallicities. Though, in some cases, more accurate metallicity values are available, we decided to use SB99 metallicities for all cases to ensure consistency.

Fig. 1 shows false-color images produced with data obtained with the Hubble Space Telescope (HST). More detail about this is presented in Sect. 2.3.1 The images show the large angular extension produced by the strong-lensing effect of magnification.

2.2. Atacama Compact Array data

This study comprises observations from three projects conducted with the Atacama Compact Array (ACA): 2018.1.01142.S (PI: González-López), 2021.2.00092.S (PI: Solimano) and 2022.1.00916.S (PI: Solimano). This array consists of twelve 7-meter radio antennae operating in interferometric mode. This generates images with a larger synthesized beam than the 12-meter array but with superior sensitivity to large-scale structures, which makes it an effective tool for detecting the apparently extended emission of molecular lines and dust continuum in giant arcs. In our study, each gravitationally lensed arc was observed in two separate bands: one for detecting CO line emission and the other for obtaining the dust continuum. We specifically targeted a single mid-j CO line for every source, with $j=3,4,5$ depending on redshift. The observations focused on bands 3 and 4 for CO, depending on the galaxy’s redshift, and bands 6 and 7 for the dust continuum. Further details of the observations are provided in Table 2.

The data was processed into spectral cubes and multi-frequency synthesis images (MFS) using the Common Astronomy Software Applications package (CASA) (CASA Team et al., 2022). Spectral cubes were made using 60 channels of 30 km s⁻¹ using the spectral windows (spw) close to the expected line. We applied a Hogbom deconvolution algorithm and a natural weighting. In contrast, the MFS images combine all channels into a single continuum image covering a bandwidth of 7.5 GHz for band 6 and 7, yielding a product suited for searching and measuring dust thermal emissions. We cleaned the image or cube using a three-sigma threshold when emission was found. We created cubes only for band 3 and 4, while MFS were cre-

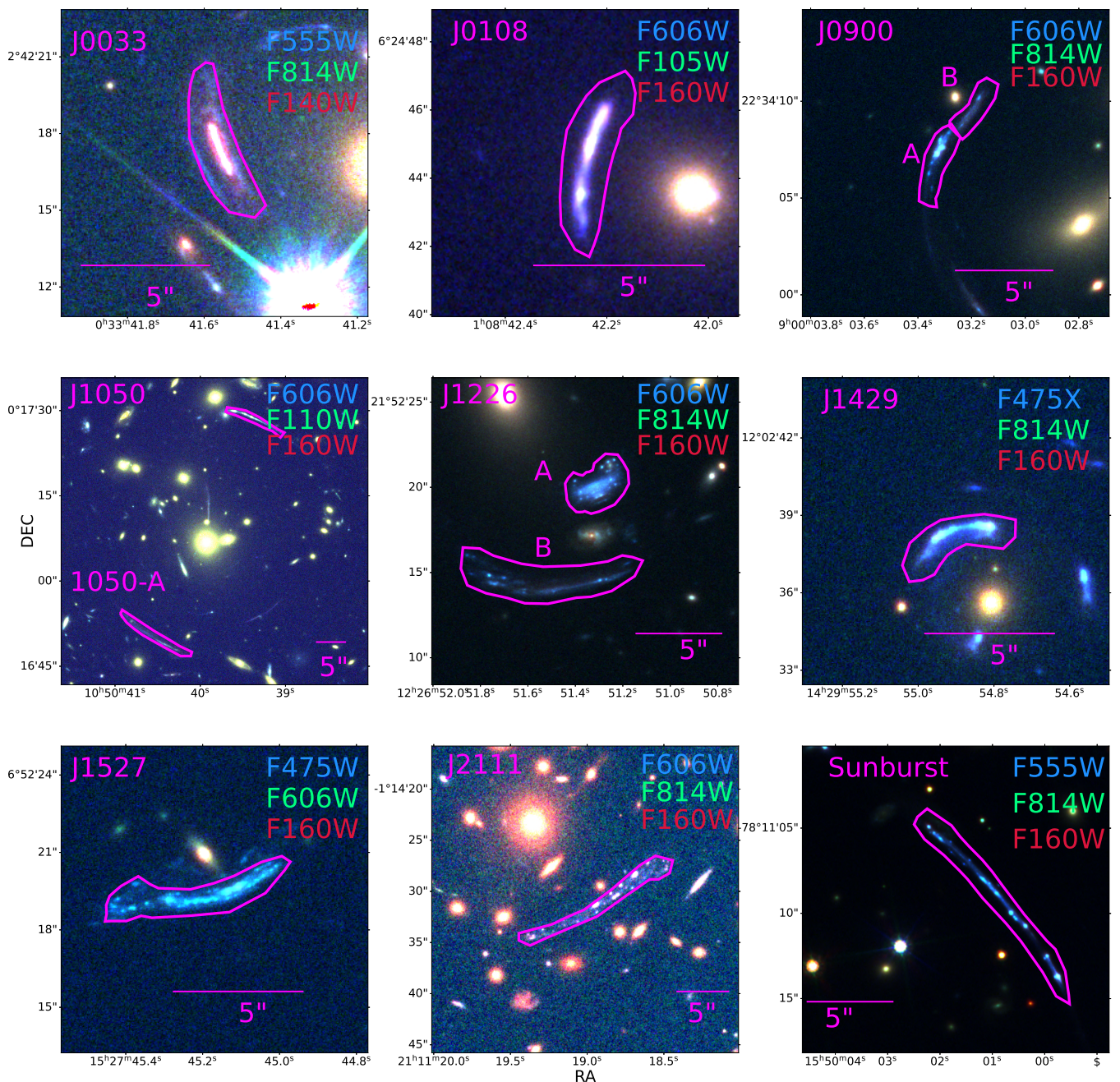


Fig. 1: Color images of gravitational arcs from the Hubble Space Telescope, labeled with target coordinates and the filters used to create them (F475X (WFC3 UVIS), F555W (WFC3 UVIS), F606W (WFC3 UVIS), F814W(WFC3 IR), F105W(WFC3 IR), F140W(WFC3 IR), F160W(WFC3 IR)).

ated for all bands. However, it is important to mention that for bands 3 and 4, the channels where emission was expected were not considered for the MFS.

2.3. Ancillary data

2.3.1. Hubble Space Telescope data

We analyzed HST images obtained through various filters and instruments to construct Spectral Energy Distributions (SEDs) for each galaxy. Data was retrieved via the Mikulski Archive for Space Telescopes (MAST). Depending on the galaxy, different instrument configurations were employed, with the Wide Field

Camera 3 (WFC3) used for infrared (IR) and ultraviolet-visible (UVIS) filters, the Advanced Camera for Surveys (ACS) for optical filters, and the Wide Field Planetary Camera 2 (WFPC2) for additional filters (F450W, F606W, F814W). The High-Level Science Products (HLSP) released by Sharon et al. (2020) were used for most arcs in this analysis. In cases where the HLSP data was unavailable, data reduced by the Hubble Advanced Products (HAP) pipeline was used instead. For the Sunburst Arc specifically, the individual HAP exposures were combined using the AstroDrizzle package. While for arc J1226, the HLSP data was obtained from the TEMPLATES program (Sharon et al., 2022b).

Table 1: Summary of the properties of the galaxies included in this study. The first column indicates the complete name of the arc, while the second column shows the abbreviation used in this work. Column 3 indicates the coordinates of each arc, and column 4 the spectroscopic redshifts. The fifth column presents the metallicity of the galaxies, and column 6 the magnification of each of the studied arcs. Column 7 indicates the discovery paper of the galaxy.

Arc	Abbreviation	Coordinates	z	$12 + \text{Log}[O/H]$	μ	Discovery
SGASJ003341.5+024217	J0033	00:33:41.55 +02:42:16.58 ⁽¹⁾	2.3900 ⁽¹⁾	8.61±0.02 ⁽²⁾	24 ⁺⁹ ₋₅	(1)
SGASJ010842.2+062444	J0108	01:08:42.21 +06:24:44.41 ⁽¹⁾	1.9099 ⁽¹⁾	8.39±0.03 ⁽²⁾	5 ⁺⁴ ₋₂	(3)
SGASJ090003.3+223408	J0900A/J0900B	09:00:03.33 +22:34:07.57 ⁽¹⁾	2.0323 ⁽¹⁾	8.27±0.02 ⁽²⁾	6 ⁺⁴ ₋₂ /8 ⁺⁵ ₋₃	(7)
SGAS J105039.6+001730 C.1	J1050	10:50:39.398 +00:17:28.78 ⁽⁶⁾	3.6258 ⁽¹⁰⁾	8.30±0.09 ⁽¹⁰⁾	72 ⁺⁹ ₋₁₀	(10)
SGAS J105039.6+001730 A.1	J1050A	10:50:40.358 +00:16:48.54 ⁽⁶⁾	2.4034 ⁽¹⁰⁾	8.30	19±1	(10)
SGASJ122651.3+215220	J1226A/J1226B	12:26:51.32 +21:52:20.00 ⁽¹⁾	2.9252 ⁽¹⁾	8.22±0.03 ⁽²⁾	84 ⁺¹³ ₋₁₀ /31 ⁺⁶ ₋₄	(8)
BG J1429+1202 B	J1429	14:29:54.857 ⁽¹⁾ +12:02:38.68	2.8241 ⁽¹⁾	8.45±0.03 ⁽²⁾	6 ⁺² ₋₁	(12)
SGAS J152745.1+065219	J1527	15:27:45.17 +06:52:19.17 ⁽¹¹⁾	2.7627 ⁽¹⁾	8.38±0.04 ⁽²⁾	12 ⁺² ₋₁	(11)
SGASJ2111118.9-011431	J2111	21:11:18.95 -01:14:31.44 ¹	2.8590 ⁽¹⁾	8.31	27 ⁺¹⁰ ₋₁₀	(9)
PSZ1G311.6518.4	Sunburst	15:49:59.83 -78:11:13.2 ⁽⁴⁾	2.3709 ⁽⁵⁾	8.43±0.03 ⁽²⁾	171 ⁽¹³⁾	(4)

References. ⁽¹⁾ Rigby et al. (2018), ⁽²⁾ Chisholm et al. (2019), ⁽³⁾ Rigby et al. (2014), ⁽⁴⁾ Dahle et al. (2016), ⁽⁵⁾ Rivera-Thorsen et al. (2017), ⁽⁶⁾ Sharon et al. (2020), ⁽⁷⁾ Diehl et al. (2009), ⁽⁸⁾ Koester et al. (2010), ⁽⁹⁾ Oguri et al. (2009), ⁽¹⁰⁾ Bayliss et al. (2014), ⁽¹¹⁾ Koester et al. (2010), ⁽¹²⁾ Marques-Chaves et al. (2017a), ⁽¹³⁾ Solimano et al. (2021)

Table 2: ACA observations information. Column 1 indicates the central frequency of the observations for both the CO band (bands 3 or 4) and the dust band (bands 6 or 7). Column 2 shows the root mean square of the observations (rms); for the CO bands, this was estimated for one channel of 30 km s⁻¹ in which emission was expected, and for the dust band, it was calculated using the MFS images, which covered 7.5 GHz. Column 3 indicates the sizes of the synthesized beams for each data product.

Arc	Central Frequency		rms		Synthesized Beam	
	CO Band [GHz]	Dust Band [GHz]	CO Band [mJy/beam]	Dust Band [mJy/beam]	CO Band [arcsec x arcsec]	Dust Band [arcsec x arcsec]
J0033	142	344	1.7	0.2	13.3×7.2	4.7×3.3
J0108	153	344	1.6	0.3	10.7×6.6	4.2×3.0
J0900	146	344	1.8	0.2	10.7×8.4	4.6×4
J1050/J1050A	95	231	1.3	0.1	16.8×10.3	7.2×4.6
J1226	140	344	1.9	0.1	10×9	4.8×3.8
J1429	96	310	2.2	0.6	18.5×12.2	5.7×3.5
J1527	98	308	1.5	0.2	18.5×11.7	6.1×3.2
J2111	96	344	1.0	0.1	10.5×8.4	5.6×4.2
Sunburst	141	344	1.5	0.2	11.5×10.9	5.0×4.7

2.3.2. James Webb Space Telescope data

To complement our study, we used James Webb Space Telescope (JWST) observations for arc J1226, which is part of the TEMPLATES program (Rigby et al., 2017). The NIRCAM observations used filters F115W, F150W, F200W, F277W, F356W, and F444W, while MIRI observations employed filters F560W and F770W. These images were reduced using scripts provided by Spilker et al. (2023). The data was used to estimate the flux of J1226 for the SED fitting. This fit can be seen in Appendix C

2.3.3. Lens models

We estimate magnification factors using parametric lens models constructed with the LENSTOOL software (Jullo & Kneib, 2009). We use the models published by Sharon et al. (2020) for most of the fields in our sample. For J0033, J1226, and the Sunburst, we use the models published by Fischer et al. (2019), Sharon et al. (2022a), and Sharon et al. (2022c), respectively. Meanwhile, the only published model for J1429 was derived from seeing-limited imaging (Marques-Chaves et al., 2017b). Hence, it suffers large uncertainties. Here, we develop a new lens model for J1429 based on the available HST data.

Since the lensing of the source in the J1429 field is dominated by a single galaxy (the brightest cluster galaxy, BCG), we chose to model the system as a single Pseudo Isothermal Elliptical Mass Distribution (PIEMD) at $z_{\text{lens}} = 0.55$ plus an external shear, instead of adding the individual cluster members as separate potentials. We keep the central coordinates of the potential fixed at $\alpha = 217.478368^\circ$, $\delta = 12.043233^\circ$, corresponding to the center of the BCG. The model is constrained by three quadruply-imaged regions of the source we identified in the color HST image (Fig. 1). We then optimize the seven free parameters of the model using LENSPOOL's Markov Chain Monte Carlo (MCMC) sampling. The marginal percentiles from the posterior distribution samples are presented in Table 3.

Table 3: Lens model parameters for the SGASJ1429 field.

Parameter	16-50-84 PDF percentiles
PIEMD potential	
$\hat{\epsilon}$	[0.19, 0.26, 0.96]
$\theta_{\hat{\epsilon}}$ ($^\circ$)	[57.06, 68.63, 71.55]
r_{core} (arcsec)	[0.19, 0.31, 0.68]
σ_{dPIE} (km/s)	[336.4, 344.2, 378.9]
r_{cut} (arcsec)	[19.0, 20.0, 47.65]
External shear	
γ	[0.171, 0.217, 0.306]
θ_{shear} ($^\circ$)	[-10.5, -7.9, -4.4]

We derived deflection matrices for all the arcs in our sample at each of the 100 model realizations drawn from the MCMC. We use the angular deflections prescribed by these matrices to bring our photometric apertures to the source plane. We then compute the mean magnification factor inside the aperture as the ratio between its image-plane and source-plane areas, μ . Finally, we use the median of the 100 samples as the nominal value and we adopt the $\sigma_\mu \equiv (p_{84} - p_{16})/2$ as the uncertainty, where p_{84} and p_{16} are the 84th and 16th percentiles, respectively. The magnifications obtained in this way are reported in Table 1 and applied to de-lensed flux-dependent quantities throughout the paper.

3. Data analysis and results

3.1. Emission lines

We searched for CO emission lines in all the targets at the expected redshifted frequencies. We manually searched the cubes to identify if any emission was detected. We considered emissions of the zeroth moment, collapsing approximately 210 km s⁻¹ around the expected/observed frequency, exceeding the 2σ level to be detections. This criterion was met for only three arcs: J0033, J0108 and J1050A. In Fig. 2, the spectra of the central regions of these arcs are depicted, with the blue line representing the 1σ noise level.

The zeroth moment maps for these arcs were obtained by collapsing the orange channels. A velocity range of 210 km s⁻¹ centered on the systemic velocity was collapsed for arcs without detections. This velocity range was chosen due to its similarity to the collapsed range for detecting J0033. The resulting zeroth moment maps were individually analyzed to derive the integrated CO fluxes of the galaxies. Two different procedures were employed, depending on whether the source was resolved or unresolved. For unresolved sources, the emission was determined as the peak value, with the images' root-mean-square (RMS) noise serving as its uncertainty. Aperture photometry

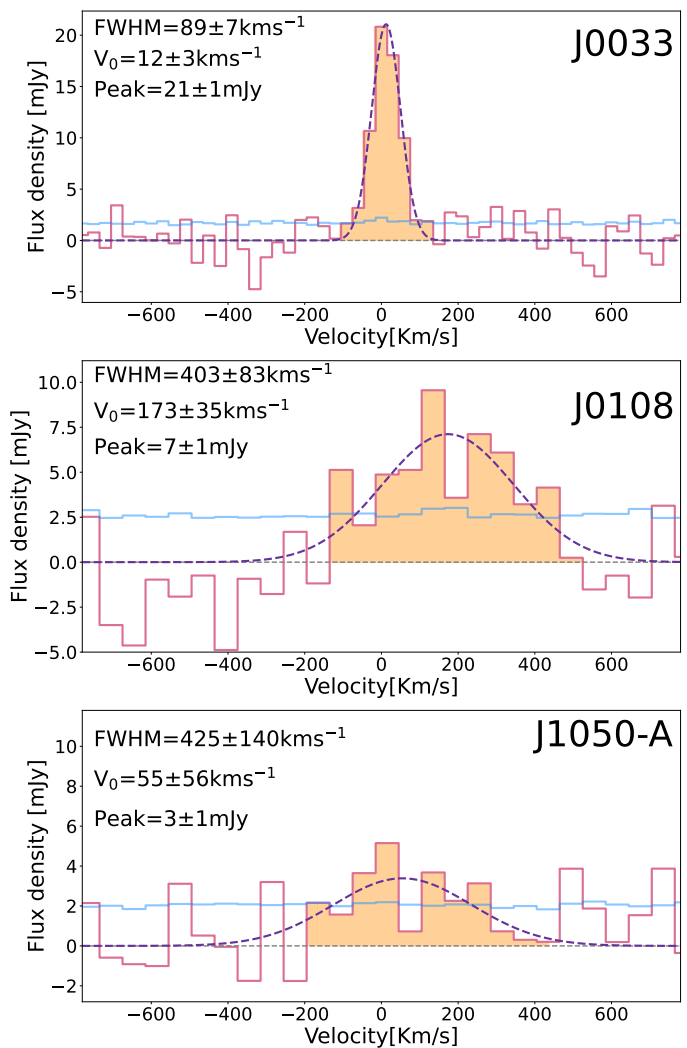


Fig. 2: CO emission detections for the galaxies J0033 (top), J0108 (middle), and J1050A (bottom). The plots are centered with velocity zero equal to the expected CO frequency. The orange channels correspond to the channels collapsed to create the zeroth moment. A Gaussian fit (purple curve) is overlaid to determine the fit parameters, Full Width Half Maximum (FWHM) in km s⁻¹, maximum amplitude [mJy], and the velocity in which the Gaussian is centered. The blue lines represent the 1σ noise level.

was performed within the galaxy region, covering one sigma emission, for resolved sources, and uncertainties were calculated using the ESSENCE code presented by Tsukui et al. (2023). This code estimates uncertainties using the autocorrelation function between pixels. The derived integrated fluxes were then used to calculate the CO luminosities of each galaxy, as presented in Table 4.

3.2. Continuum data

We investigated the dust continuum emission from the galaxies by using MFS images, which consider all spw. This enables the extraction of integrated continuum fluxes for each arc. Continuum detections were identified when the emission exceeded a 2σ significance level. The arcs and their ACA dust continuum

Table 4: Table of integrated CO line fluxes and derived CO luminosities for each galaxy. Listed are the galaxy names, CO transition line, unmagnified integrated flux (Jy km s^{-1}), and unmagnified calculated CO luminosity ($\mu L'_{\text{CO}}$ in units of $10^{10} \text{ K km s}^{-1} \text{ pc}^2$). Statistic uncertainties on the measured values are included, with upper limits being considered at the three σ significance level

Arc	CO Transition	$\mu\Delta\nu S_\nu$ [$\text{Jy} \cdot \text{Km s}^{-1}$]	$\mu L'_{\text{CO}}$ [$10^{10} \text{K km s}^{-1} \text{ pc}^2$]
J0033	(4-3)	2.0 ± 0.1	3.4 ± 0.2
J0108	(4-3)	1.3 ± 0.4	1.4 ± 0.4
J0900A	(4-3)	<0.5	<0.6
J0900B	(4-3)	<0.5	<0.6
J1050	(4-3)	<0.3	<1.2
J1050A	(3-2)	0.4 ± 0.1	1.2 ± 0.3
J1226A	(5-4)	<0.4	<0.7
J1226B	(5-4)	<0.2	<0.4
J1429	(3-2)	<0.4	<1.7
J1527	(3-2)	<0.4	<1.6
J2111	(3-2)	<0.2	<0.9
Sunburst	(4-3)	<0.4	<0.6

data are depicted in Fig. 3. Flux measurements for the arcs were conducted using the same procedures employed for obtaining the fluxes of the zeroth moment maps. The derived continuum flux densities, expressed in mJy, are listed in Table 5.

3.3. SED fitting

In this study, we employed the Code Investigating GALaxy Emission (CIGALE; Boquien et al. 2019) to perform SED fitting. CIGALE operates on the principle of energy balance, where the energy absorbed by dust is re-emitted in the infrared spectrum. We provided CIGALE with each galaxy's redshift and HST, ALMA, and JWST photometry. Specifically, we adopted a delayed star formation history and used the Bruzual & Charlot (2003) simple stellar population model. Additionally, we accounted for nebular emission and dust attenuation, employing the Charlot & Fall (2000) attenuation law and the dust templates proposed by Dale et al. (2014).

Our approach involved two stages of SED fitting for each galaxy: one considering the entire arc and another focusing on resolved properties. The latter enabled a robust estimation of the surface star formation rate density (Σ_{SFR}) for each region. Aperture photometry was performed on HST images at various wavelengths for the whole arc, supplemented by ALMA Band 6 or 7 when available. The apertures used were created to cover the highest percentage of the galaxy's flux in the reddest available HST filter and are presented in Fig. 1. The flux percentages covered can be seen in Appendix F. An illustrative example of a SED fit is presented in Fig. 4, and the parameters' details used are shown in Appendix E. Table 5 presents the values derived from the fit.

We calculated the SFR for several circular apertures for the resolved analysis and normalized them by the corresponding area to derive Σ_{SFR} values. This approach facilitated the characterization of a Σ_{SFR} distribution across different regions of the galaxies. We considered the median of the distribution as a

representative value of the total Σ_{SFR} of the galaxy.

3.4. Dust mass

We used the dust continuum observations to constrain the dust mass of our targets. Our estimates applied the equations in Casey et al. (2019):

$$M_{\text{dust}} = \frac{S_{\nu_{\text{obs}}} D_L^2 (1+z)^{-(3+\beta)}}{\kappa(\nu_{\text{ref}}) B_\nu(\nu_{\text{ref}}, T_d)} \left(\frac{\nu_{\text{ref}}}{\nu_{\text{obs}}} \right)^{2+\beta} \left(\frac{\Gamma_{\text{RJ}}(\text{ref}, 0)}{\Gamma_{\text{RJ}}} \right) \quad (2)$$

In this equation, $\kappa=1.3 \text{ cm}^2 \text{ g}^{-1}$ represents the dust-mass absorption coefficient, $\beta=1.8$ denotes the emissivity spectral index, and $T_d=25 \text{ K}$ signifies the global mass-weighted dust temperature (Scoville et al., 2016). The Γ_{RJ} values serve as corrections to the Planck function, B_ν , accounting for the Rayleigh-Jeans deviation (Scoville et al., 2016). These values can be estimated using Equation 3, where h denotes Planck's constant and k represents the Boltzmann constant. In this equation, we also use $T_d=25 \text{ K}$.

$$\Gamma_{\text{RJ}}(T_d, \nu, z) = \frac{h\nu(1+z)/kT_d}{e^{h\nu(1+z)/kT_d} - 1} \quad (3)$$

In the upper section of Equation 2, Γ_{RJ} is computed utilizing the reference frequency and redshift of 0, whereas, in the lower section, it is calculated using the observed frequency and redshift. It is important to note that this equation is applicable only when $\lambda_{\text{rest}} > 250 \mu\text{m}$, as this is the Rayleigh-Jeans tail, where dust is optically thin (Scoville et al., 2016), limiting our ability to estimate the dust mass in Band 7 for certain arcs. However, the dust temperature is higher in the case of low-metallicity galaxies, which displaces the Rayleigh-Jeans tail towards shorter wavelengths, allowing us to use this method for more galaxies of our sample (Saintonge et al., 2013). We considered the limit to be J1226A/B as it has a rest wavelength of $222 \mu\text{m}$. The only galaxy with a higher redshift is J1050. However, as it was observed at 1.25 mm , it can still be studied in this context.

3.5. Stacking

Given our sample size, we were able to stack the CO and dust continuum emissions for our observations. This allowed us to study the average behavior of our sample. In all cases, we observed that the signal-to-noise ratio was optimized when galaxies were weighted by $1/\sigma^2$, where σ^2 represents the data variance. Since the galaxies were gravitationally lensed, we applied a magnification correction to all fluxes and images before stacking them. This ensured that our final results represented the intrinsic properties of the galaxies, such as the molecular gas values for each stack.

For CO emissions, we obtained the spectra of a single central pixel for each galaxy, which we then stacked. Each spectrum was corrected by the primary beam and then changed to consider the expected frequency as the systematic velocity of 0.0. This expected frequency depended on the observed j transition ($j=3,4,5$) and the systematic redshift. We first stacked all the arcs and then repeated the process, excluding galaxies J0033, J0108, and J1050A, which had detections. This gave us insight into the behavior of the undetected galaxies. These samples will be referred to as *All Arcs* and *Non-detections*, respectively. Table 6 reports the obtained flux values for each

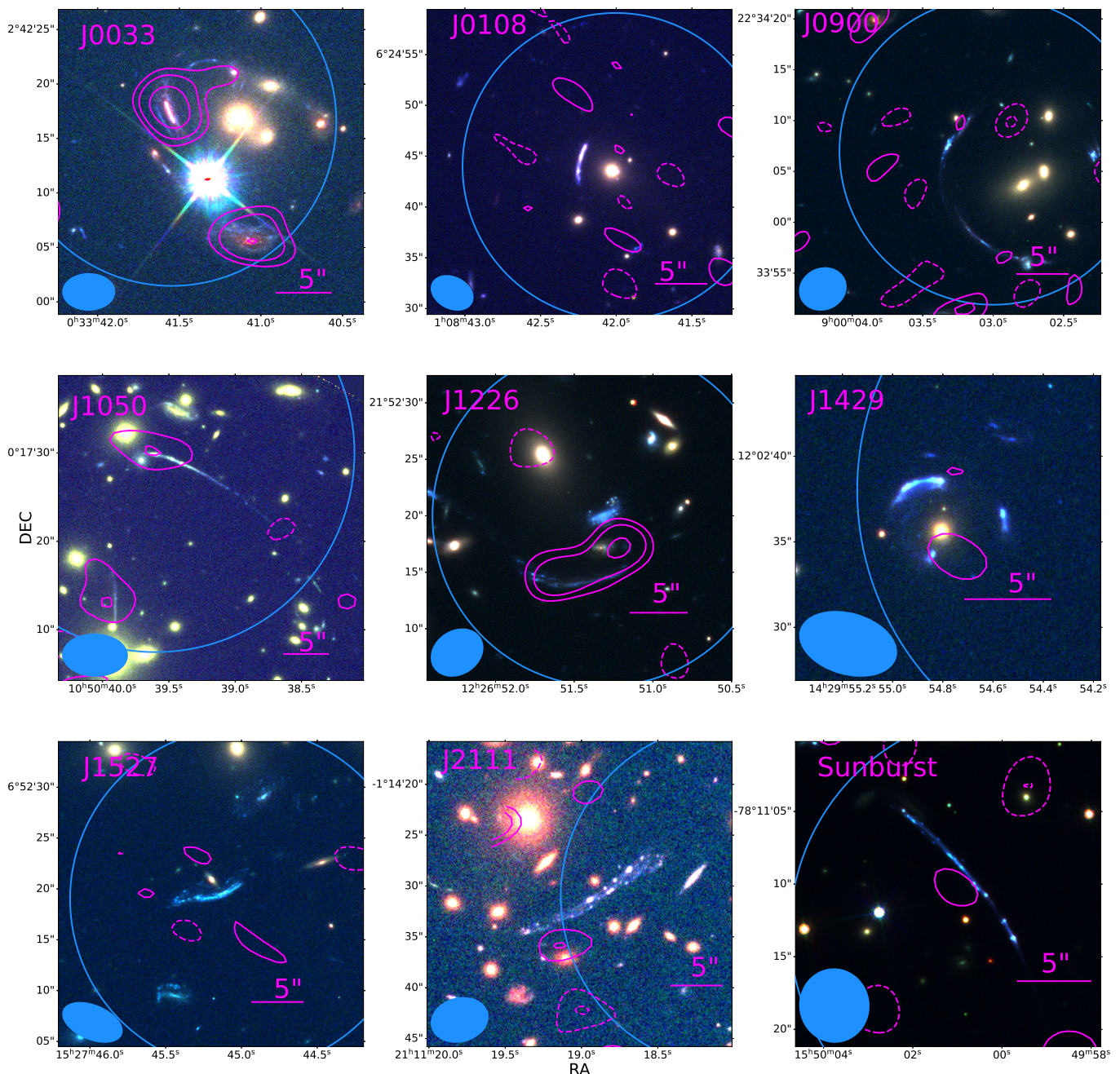


Fig. 3: The text describes Hubble Space Telescope color images of gravitational arc systems with overlaid contours showing dust continuum emission observed with ALMA at different sigma levels (-5,-3,-2,2,3,5), dashed lines correspond to negative values while solid lines are positive values. The sizes of the synthesized beams are indicated in the bottom left corners of the images. Additionally, the large circles represent ALMA’s primary beam, each equal to 0.5 for the respective target fields.

case. We considered emission to be significant if the integrated flux density of the orange area surpassed 1.5σ , calling these tentative detections. Both stacked spectra can be observed in Fig 5; here, we can observe that both are similar, which indicates the same spectrum dominates both stackings. We used the individual galaxy properties and the weights to obtain representative properties of the stacks, which were then used to estimate the molecular masses. For this, we did a weighted average of the galaxy properties using $1/\sigma^2$ as the weight. All values derived from the stacks are presented in Table 6.

Regarding the continuum, we performed single-pixel stacking. Observations were divided into bands 3 and 4 (B3/4) and 6 and 7 (B6/7); as a final result, we obtained three stacks. Firstly, we stacked all the galaxies for bands 3 and 4, referred to as *Continuum B3/4 all arcs*. Then we did the same with bands 6 and 7, referred to as *Continuum B6/7 all arcs*. Finally, we removed all arcs with detections in bands 6 and 7 and created the stack *Continuum B6/7 non-detections*. We estimated the fluxes using the single-pixel method, presented in Table 6, and then used the errors to weigh the properties of the galaxies; the average properties can be found in Table 6. We only obtain a significant detection (over 1.5σ) for the *Continuum B6/7 all arcs*. We were

Table 5: The table presents the dust continuum flux obtained from ACA data and the parameters obtained from the SEDs. Column 2 presents the dust continuum magnified values. Columns 3, 4, and 5 show demagnified values of stellar mass, star formation rate, and superficial star formation rate density, respectively.

Arc	μS_ν [mJy]	$\text{Log}(M_*)$ [M_\odot]	$\text{Log}(\text{SFR})$ [$M_\odot \text{yr}^{-1}$]	Σ_{SFR} [$M_\odot \text{yr}^{-1} \text{kpc}^{-2}$]
J0033	3.7 ± 0.4	10.7 ± 0.3	1.8 ± 0.3	1.3 ± 0.3
J0108	< 0.4	10.4 ± 0.3	1.7 ± 0.3	0.23 ± 0.3
J0900A	< 0.5	9.7 ± 0.3	1.2 ± 0.2	0.8 ± 0.2
J0900B	< 0.4	9.8 ± 0.3	1.0 ± 0.2	1.2 ± 0.5
J1050	0.4 ± 0.1	9.8 ± 0.2	1.2 ± 0.1	1.5 ± 0.2
J1050A	-	10.0 ± 0.2	1.5 ± 0.2	0.35 ± 0.03
J1226A	< 0.3	9.5 ± 0.1	0.8 ± 0.1	1.4 ± 0.1
J1226B	0.8 ± 0.2	10.0 ± 0.2	1.3 ± 0.2	0.49 ± 0.03
J1429	< 2.5	10.6 ± 0.3	1.9 ± 0.2	46 ± 11
J1527	< 0.5	10.2 ± 0.6	1.5 ± 0.2	10 ± 4
J2111	< 1.0	10.0 ± 0.3	1.2 ± 0.2	0.23 ± 0.01
Sunburst	< 1.0	9.5 ± 0.1	0.9 ± 0.1	0.52 ± 0.03

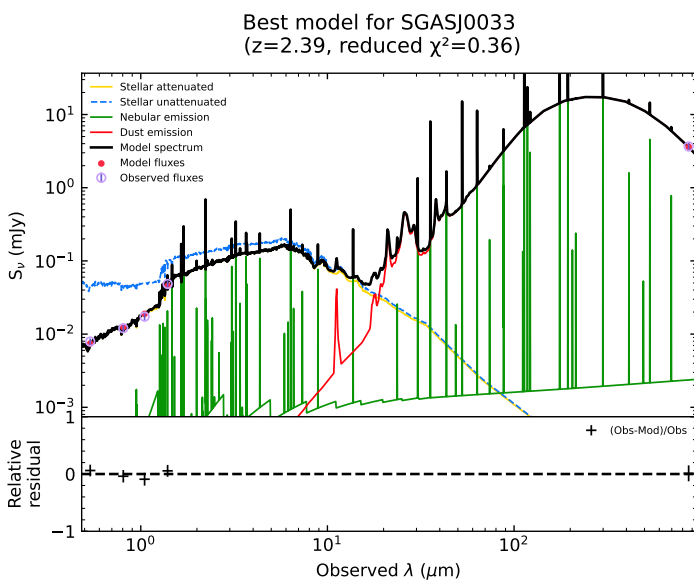


Fig. 4: SED fit for the galaxy J0033 using HST and ALMA photometry. The fit was modeled with CIGALE to derive the physical properties of the galaxy.

able to obtain dust masses for the continuum stack as the stacked properties fulfilled the requirement $\lambda_{\text{rest}} > 250 \mu\text{m}$.

3.6. Molecular gas mass

3.6.1. Molecular gas mass using CO emission

Since we are working with sub-solar metallicities, we decided to employ an α_{CO} model that accounts for the photo-dissociation of molecular gas in these types of galaxies (Genzel et al., 2015). Thus, we selected the first model (a) proposed in Genzel et al. (2015). We also took into consideration the Accurso et al. (2017) model as it was created for galaxies with similar metallicities (Accurso et al., 2017). However, as all the scaling relations we used to compare our data were derived using the Tacconi et al. (2018) model, a similar model such as Genzel et al. (2015) was considered more adequate.

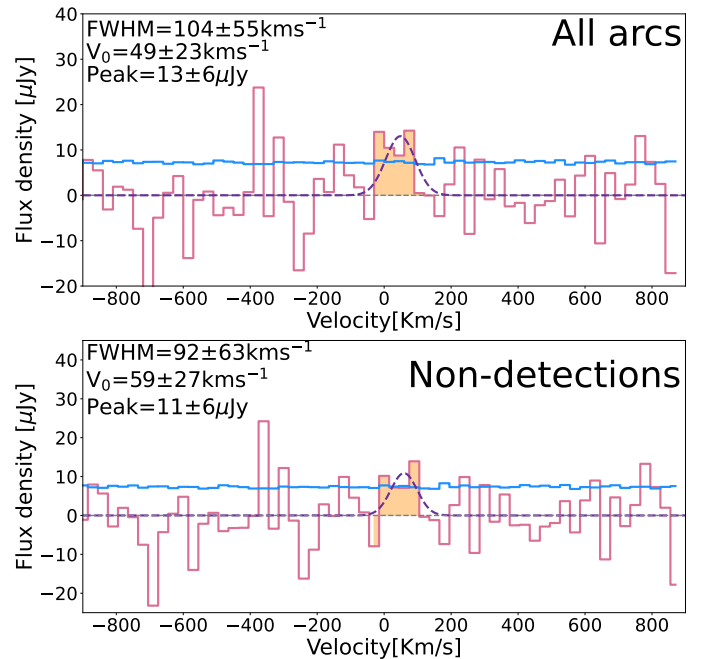


Fig. 5: The top panel shows the CO stack for all the arcs, while the bottom panel shows the CO stack for the galaxies with no detection. A Gaussian fit was performed in both cases and is overlaid in purple. The blue lines represent the $1\text{-}\sigma$ noise level, while the orange region indicates the channels collapsed to obtain the integrated fluxes.

To obtain the molecular gas, we must use Equation 1, which only applies to CO(1-0). As we are working with other j transitions ($j=3,4,5$), an additional conversion factor (r_{ji}) is required. We define r_{j1} as Equation 4. Where $L'_{\text{CO}(j-(j-1))}$ and $L'_{\text{CO}(1-0)}$ are the CO luminosities in the transitions $j-(j-1)$ and 1-0 respectively. For this study, we obtained relationships for r_{51} , r_{41} , and r_{31} , which enabled us to determine the CO(1-0) luminosity for each arc.

$$r_{j1} = \frac{L'_{\text{CO}(j-(j-1))}}{L'_{\text{CO}(1-0)}} \quad (4)$$

Table 6: Stacking results for CO and continuum emissions, including intrinsic properties for the composite galaxy. Column 2 displays the integrated flux, Column 3 displays the flux, Column 4 displays the redshift, Column 5 displays the molecular gas mass, Column 6 displays the logarithm of stellar mass, and Column 7 displays the logarithm of the star formation rate.

Stacking	$\Delta\nu S_\nu$ [mJy · Km s ⁻¹]	S_ν [μJy]	z	M_{mol} [10 ⁸ M _⊙]	Log(M _*) [M _⊙]	Log(SFR) [M _⊙ yr ⁻¹]
CO all arcs	1.6±0.7	-	2.67	2.1 ^{+0.9} _{-0.8}	9.6±0.09	0.96±0.07
CO some arcs	1.2±0.8	-	2.69	1.9±1.2	9.59±0.09	0.95±0.07
Continuum B3/4 all arcs	-	<1.2	2.75	<340	9.6±0.09	0.98±0.07
Continuum B6/7 all arcs	-	4.9±0.9	2.96	22.5 ,5	9.6±0.1	1.0±0.1
Continuum B6/7 some arcs	-	4±2	2.90	12 ± 6	9.59±0.07	0.9±0.1

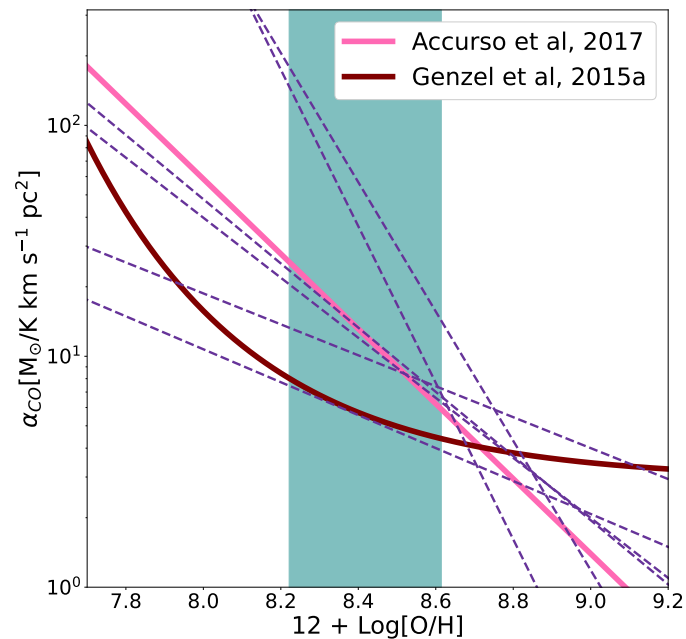


Fig. 6: Comparison of different α_{CO} models across varying metallicities. The shaded region indicates the metallicity range of our sample. Dashed lines show several models which were not considered for this work. (Wilson, 1995; Magdis et al., 2011; Genzel et al., 2012; Schrubba et al., 2012; Genzel et al., 2015; Accurso et al., 2017; Tacconi et al., 2018; Madden et al., 2020)

Studies such as Narayanan & Krumholz (2014) have proposed a relationship between Σ_{SFR} and r_{j1} , as this parameter serves as a tracer of temperature and density, both of which influence the CO spectral line energy distribution (SLED) (Narayanan & Krumholz, 2014). In their study, Narayanan & Krumholz (2014) used models based on resolved and unresolved simulations across various values of j to obtain relationships between these quantities. These models are presented as purple lines in Fig. 7 and Fig. 8. As a way to obtain more realistic results, we decided to compile an observational dataset (Taniguchi & Ohyama, 1998; Papadopoulos et al., 2012; Riechers et al., 2013; Daddi et al., 2015; Hatsukade et al., 2019; Brisbin et al., 2019; Kaur et al., 2022; Henríquez-Brocal et al., 2022; Lenkić et al., 2023; Castillo et al., 2023) for different r_{j1} values and their respective Σ_{SFR} . This dataset can be found in Appendix D. We fitted a model to the observational data sets for $j=3,4$ and derived relations between r_{31} and r_{41} with Σ_{SFR} , which are illustrated in Fig. 7 and Fig. 8 respectively. These relations were then used to estimate the corresponding r_{j1} values using the Σ_{SFR} obtained by the SED fits. As the observational models are

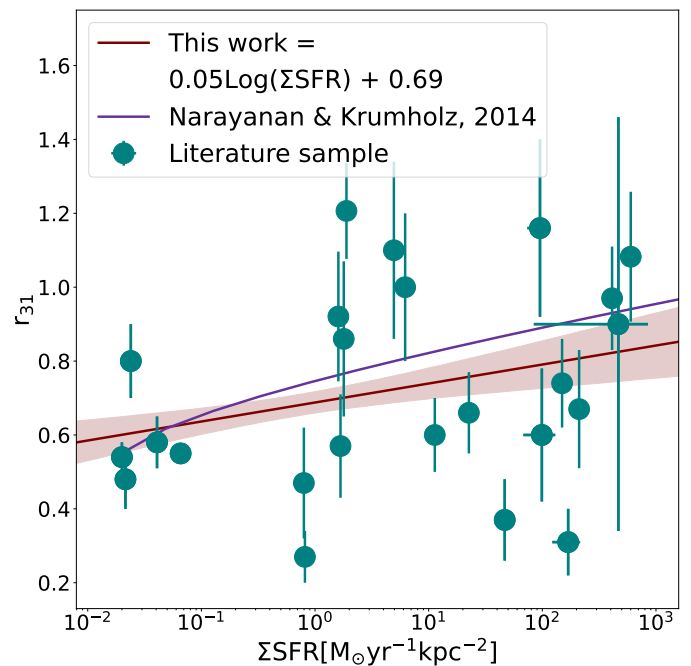


Fig. 7: Relationship between Σ_{SFR} and r_{31} . Green dots denote data points used in constructing our model. The brown line represents our estimated model with a 1σ error range, while the purple line depicts the Narayanan & Krumholz (2014) model for unresolved sources.

consistent with the simulated models by Narayanan & Krumholz (2014), for the case of r_{51} , where insufficient observational data was available, we opted to apply this simulated model.

Finally, by using the obtained α_{CO} and Equation 1, we were able to determine the corresponding molecular gas masses. The magnification-corrected masses are reported in Table 7, along with the respective r_{j1} and α_{CO} values.

3.6.2. Molecular gas mass obtained with dust mass

We also derived the molecular gas mass by relating it to the dust mass using the gas-to-dust ratio (δ_{GDR}). This value is as uncertain as α_{CO} and depends on metallicity. The model used exhibits a power-law dependency on metallicity: $\delta_{GDR} = Z^\gamma$ (Tacconi et al., 2018). We adopted the calibration suggested in Tacconi et al. (2018), where $\delta_{GDR}(Z_\odot) = 100$ and $\gamma = 0.85$. We then derived values for the molecular gas mass for each galaxy from the metallicities reported in Table 1 and the dust masses by using Equation 5. Table 7 presents the magnification-corrected

Table 7: Molecular gas masses derived from CO emission and dust continuum, corrected for magnification and accompanied by the specific parameters utilized for each arc. Column 2 indicates the α_{CO} conversion factor used for the calculation. Columns 3 to 5 show the r_{j1} values for $j=3,4,5$. Column 6 displays the molecular gas mass obtained using CO, column 7 the molecular gas mass obtained using 2.1mm/3.1mm dust continuum and column 8 the molecular gas mass obtained using 870 $\mu\text{m}/1.25\text{mm}$ dust continuum.

Arc	α_{CO}	r_{31}	r_{41}	r_{51}	M_{mol} CO [$10^9 M_{\odot}$]	M_{mol} (2.1mm/3.1mm) [$10^9 M_{\odot}$]	M_{mol} (870 $\mu\text{m}/1.25\text{mm}$) [$10^9 M_{\odot}$]
	[$M_{\odot}(\text{Kkms}^{-1}\text{pc}^{-2})^{-1}$]						
J0033	4.4	-	0.62	-	10 ± 3	<157	22^{+7}_{-6}
J0108	5.8	-	0.49	-	29^{+20}_{-14}	<1914	<16
J0900A	7.2	-	0.58	-	<11	<1239	<21
J0900B	7.2	-	0.61	-	<8	<955	<13
J1050	6.8	0.63	-	-	<1.7	<239	6 ± 2
J1050-A	4.9	0.52	-	-	6 ± 1	<1070	-
J1226A	8.1	-	-	0.28	<2.2	<84	<1
J1226B	8.1	-	-	0.23	<4.1	<111	8 ± 2
J1429	5.3	0.78	-	-	<18	<4442	<74
J1527	5.9	0.75	-	-	<10	<2274	<9
J2111	4.7	0.67	-	-	<2.4	<394	<6
Sunburst	5.5	-	0.55	-	<0.4	<26	<1.3

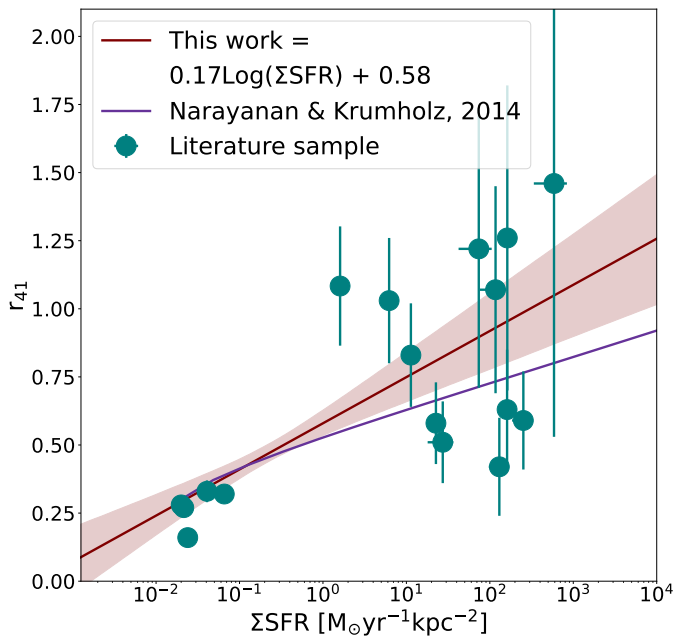


Fig. 8: Same as Fig. 7 but for r_{41}

molecular gas masses.

$$M_{\text{mol}} = 100M_{\text{dust}}(Z^{-0.85}) \quad (5)$$

3.6.3. Molecular gas comparison

We determined the molecular gas masses using three distinct methods; the corresponding results are presented in Fig. 9. We can observe that the least restrictive method was the molecular gas mass obtained from the dust mass at 2.1/3.1 mm, which corresponds to data from bands 3 and 4. These values are also upper limits, meaning they agree with the results of the other methods. On the other hand, the most constraining method is the estimation using CO emission. This CO-based approach is also generally consistent with the dust mass method at 870 $\mu\text{m}/1.25\text{mm}$ (bands 6 and 7), which provides an intermediate value when measured. The pink arrow in Fig. 9 corresponds

to the median value of how much the CO points would move upwards if we had used the Accurso et al. (2017) model for α_{CO} , instead of Genzel et al. (2015). In the figure, all detections (surrounded by a red edge) have statistic error bars; however, they are not always visible due to the large range covered by the y-axis.

For the remainder of the study, we primarily used CO-based molecular gas estimates, as they are known to only trace the molecular gas, while dust masses could also trace atomic gas (Scoville et al., 2014). While the dust-based masses provide useful upper limits, the CO-derived masses are expected to be more accurate, as they directly trace the molecular gas content.

4. Discussion

4.1. The galaxies in our sample in context

We selected datasets from recent studies to contextualize our galaxies within the current scientific landscape. Firstly, we used a sample of 137 high-redshift ($z > 2$) SFGs from the PHIBSS catalog (Tacconi et al., 2018), primarily located on the main sequence and spanning a stellar mass range of $\sim 10^{9.8} - 10^{11.8} M_{\odot}$. Secondly, we included the complete xCOLD GASS catalog (Saintonge et al., 2017) consisting of 306 galaxies at approximately $z \sim 0$, covering a stellar mass range of $\sim 10^9$ to $10^{11.3} M_{\odot}$.

We also incorporated a sample of strongly lensed SFGs from four studies (Saintonge et al., 2013; Dessauges-Zavadsky et al., 2015; Motta et al., 2018; Tsujita et al., 2024). This sample covers a redshift range between 1.4 and 3.65 and $\text{Log}(M_*/M_{\odot})$ between 9.26 and 11.49. All measurements of molecular gas mass estimates were obtained using CO emission. To ensure consistency and to enable a robust comparison, we changed the α_{CO} parameter used for the data to the Genzel et al. (2015) value.

Additionally, we included data on galaxies identified as *main sequence starbursts* (MS SBs) by Gómez-Guijarro et al. (2022). These galaxies were selected from the ALMA-GOODS 2.0 survey, which comprises low-resolution 1.1 mm observations that covered a redshift range between 1.314 and 4.73. The main sequence starbursts were identified based on their deviation from the main sequence by a maximum of $\Delta\text{MS} \equiv \text{SFR}/\text{SFR}_{\text{MS}} \equiv 3$,

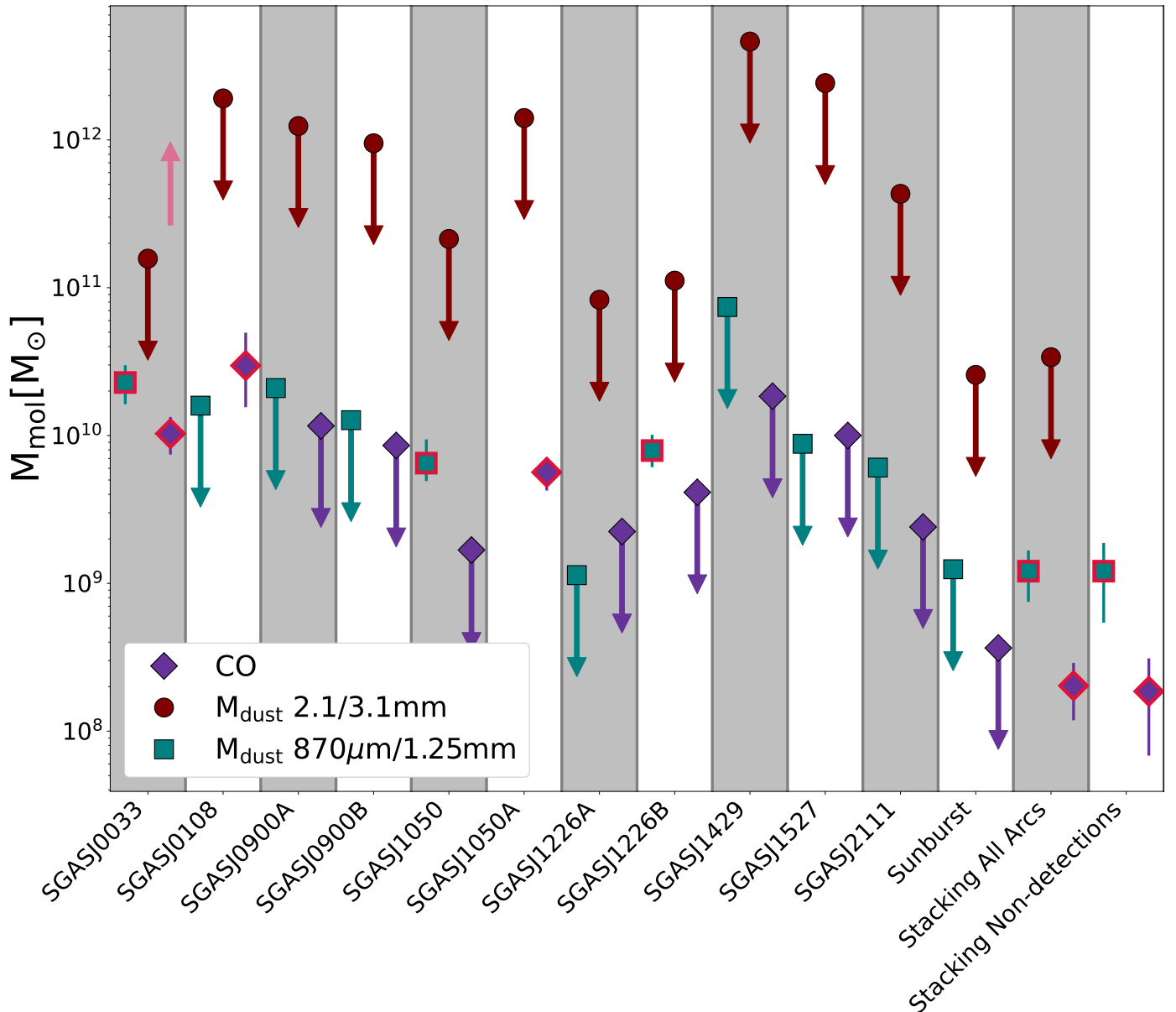


Fig. 9: Comparison of the molecular gas mass estimates using the three methods discussed in the text. The pink arrow corresponds to how the CO points would be displaced if we had used the Accurso et al. (2017) model for α_{CO} . The stacking samples were created using weighted averages with weights $1/\sigma^2$. The stacking all arcs considered all arcs, while stacking non-detections only considered arcs in which no detection was present. Markers with a red edge and errorbars indicate detections.

and their gas masses were derived using the dust mass. Even though they belong to the MS by selection, they are denominated starbursts due to their short gas depletion timescales.

In Fig. 10, we present the data from our study alongside the recent literature values, comparing them to the main sequence relationship at redshift 2.5 derived from Speagle et al. (2014). Notably, all our galaxies and stacking values fall within the MS, indicating that we are dealing with typical MS star-forming galaxies from the epoch.

The ratio between molecular gas mass and stellar mass, known as the gas fraction (μ_{gas}), offers insights into the relative abundance of molecular gas compared to stellar mass within galaxies, i.e., gas already converted into stars. In Fig 11, we depict how this ratio varies with stellar mass. The brown line represents the scaling relation for main-sequence galaxies

established by Tacconi et al. (2018). This model was chosen to compare as it was seen to be the one that best follows the CO-based observations at the studied redshifts (Sanders et al., 2023).

Our analysis reveals that most of our galaxies align with or fall below the scaling relation, with some below even representing upper limits, thus not adhering to the relation. Notably, the gas fractions observed in our study are comparable to those reported in Gómez-Guijarro et al. (2022), albeit with significantly lower stellar masses. While some lensed sources (Saintonge et al., 2013; Dessauges-Zavadsky et al., 2015; Motta et al., 2018; Tsujita et al., 2024) agree with our targets, others lie on or above the scaling relation. Most of the sources with similar gas fractions to our sample have similar masses,

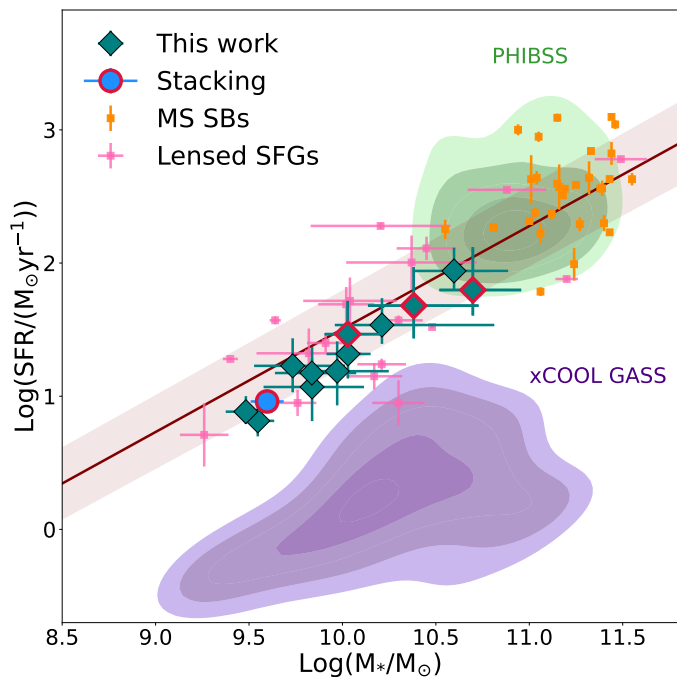


Fig. 10: SFR as a function of stellar mass. The brown line denotes the main sequence at redshift 2.5 established by Speagle et al. (2014). Pink markers represent lensed SFG (Saintonge et al., 2013; Dessauges-Zavadsky et al., 2015; Motta et al., 2018; Tsujita et al., 2024), while orange markers are MS SBs from Gómez-Guijarro et al. (2022). The purple contours are density plots of the xCOOL GASS data, while the green contours are the PHIBSS data Tacconi et al. (2018). Teal markers indicate the galaxies from this work; when they have a red edge and error bars, they represent detections.

which could indicate that at lower masses, this is a normal value. Additionally, galaxies derived from our stacking analysis appear to fall below the relationship. The stacking represents a low-mass galaxy with low metallicity, thus suggesting that lower-mass lensed galaxies may exhibit lower molecular gas fraction compared to their higher-mass counterparts

The depletion time, defined as the ratio of molecular gas mass (M_{mol}) to SFR, provides insight into how long a galaxy can sustain its current level of star formation activity in the absence of new material. In Fig. 12, we illustrate how this property varies with redshift, with the brown line representing the scaling relationship proposed by Tacconi et al. (2018). This model was chosen as it was seen to be the one that best follows the CO-based observations at the studied redshifts (Sanders et al., 2023). Our analysis reveals that most of our data points fall below this relationship, with some upper limits extending beyond it, suggesting that the targeted galaxies are experiencing accelerated depletion of their molecular gas reservoirs and are likely running out of fuel for star formation more rapidly than typical galaxies at similar redshifts. These findings are consistent with those reported in Gómez-Guijarro et al. (2022) and with what is observed in some lensed galaxies. However, other lensed galaxies (Saintonge et al., 2013; Dessauges-Zavadsky et al., 2015; Motta et al., 2018; Tsujita et al., 2024) appear to be above this relationship. Furthermore, the data points from our stacking analysis also fall below the scaling relation, indicating that, on average, our galaxies exhibit relatively short depletion

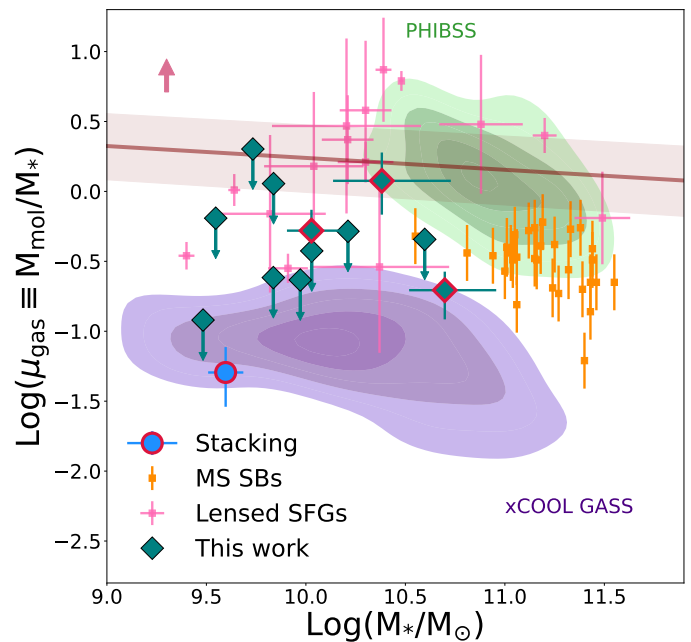


Fig. 11: Same as Fig. 10 but for the gas fraction as a function of stellar mass. The brown line denotes the scaling relation established by Tacconi et al. (2018) for main sequence galaxies. The pink arrow corresponds to how much the CO points would move upwards if we had used the Accurso et al. (2017) model for α_{CO} .

times. This suggests that the studied galaxies, as a whole, are undergoing rapid consumption of their molecular gas reservoirs.

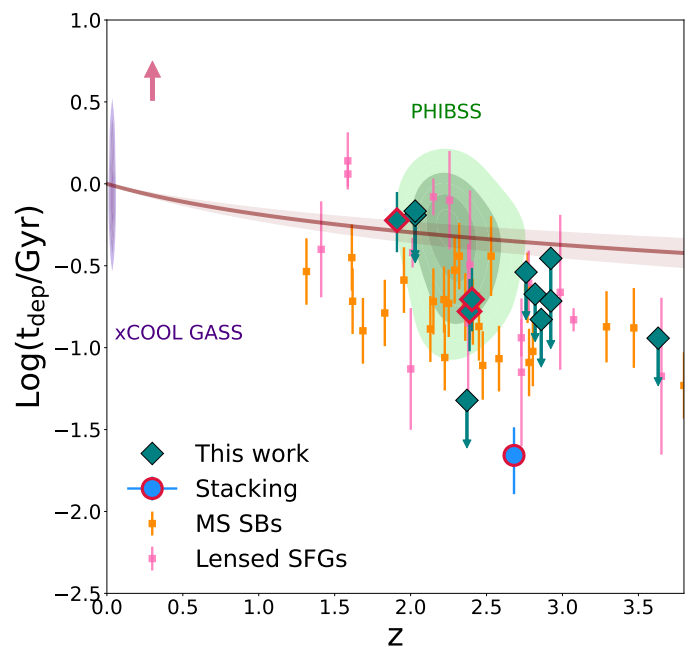


Fig. 12: Same as Fig. 10 but for depletion time as a function of redshift. The brown line represents the scaling relationship established by Tacconi et al. (2018). The pink arrow corresponds to how much the CO points would move upwards if we had used the Accurso et al. (2017) model for α_{CO} .

4.2. Interpretation and possible caveats

The low depletion times and gas fractions observed in the studied galaxies may indicate a molecular gas deficit within these systems, given that the SFRs are consistent with being in the star-forming MS. This characterization aligns with the findings reported by Gómez-Guijarro et al. (2022), who identified similar properties in galaxies they classified as MS SB. Despite being located on the main sequence, these galaxies exhibited low depletion times and low gas fractions. In this study, we propose several possibilities to explain the observed deficit and discuss the validity of each scenario.

One possibility to explain the apparent gas deficit is that there are very large systematic errors in the estimation of the molecular gas masses. As shown in Fig. 6, there are several recipes for estimating α_{CO} . We can observe that the Genzel et al. (2015) model adopted in our study provides one of the lowest values for α_{CO} at the studied metallicities. If we had used other models that also account for photodissociation, such as Madden et al. (2020), the α_{CO} values would be larger, resulting in higher molecular gas mass estimates. Thus, the gas fractions would be higher by approximately one dex. However, the Madden et al. (2020) model was not chosen as its values were suggested to be upper limits rather than realistic estimates in Ramambason et al. (2024). Another model considered was Accurso et al. (2017), which would cause the gas deficit to disappear. However, considering that the scaling relationships were created using α_{CO} values similar to Genzel et al. (2015), if we were to reestimate the scaling relations to use the Accurso et al. (2017) values, there is a probability that the deficit may still appear.

We also considered the possibility that lower-mass galaxies have a more extensive atomic gas reservoir relative to their molecular gas reservoir. In both our study and the ones used for comparison, the gas fraction was approximated from $\mu_{\text{gas}} = (M_{\text{mol}} + M_{\text{atomic}})/M_*$ to $\mu_{\text{gas}} \sim M_{\text{mol}}/M_*$, as this is considered valid at $z > 0.4$ (Tacconi et al., 2018). It is essential to consider that with increasing mass, the fraction of molecular gas compared to atomic gas increases, meaning lower mass galaxies should contain a higher fraction of atomic gas (Popping et al., 2014; Lagos et al., 2015). As Tacconi et al. (2018) only studies high-mass galaxies at high redshifts, the simplification is valid for their study, and the scaling relations should not vary if we consider the complete definition of μ_{gas} . Interestingly Messias et al. (2024) found there might be evidence for an increasing atomic gas reservoir between the redshifts $z \sim 1.5$ and $z \sim 2.5$, which could indicate that cosmic noon galaxies have higher atomic gas reservoirs. As our galaxies are low-mass galaxies at cosmic noon, a relatively higher atomic gas content could be a suitable explanation for the observed deficit. A way of estimating the atomic gas mass would be with the molecular gas mass obtained using the dust observations, as initially Scoville et al. (2014) considered the gas obtained with dust masses to be composed of both atomic and molecular gas. As we obtained two different dust masses from our stacked galaxy, representing a low-mass galaxy at cosmic noon. We decided to use the 870 $\mu\text{m}/1.25\text{mm}$ dust continuum and CO molecular gas masses of the *All galaxies* stacks and compare them. From this, we obtained that the molecular mass estimated with CO was only 9% of the molecular mass obtained with the dust mass. Meaning that possibly 91% of the gas is in atomic form.

Another possible explanation for the apparent observed gas deficit is the presence of what is known as CO-dark gas. Reduced dust abundance permits UV radiation to photodissociate CO molecules more effectively at low metallicities, such as in the

galaxies under study. Consequently, while H_2 remains shielded from photodissociation, we are left with the same amount of molecular gas but with only a central CO core and a [C I] cloud (Madden et al., 2020). This scenario implies that CO may not serve as an effective tracer for the entire molecular gas content, potentially capturing less than 30% of the gas present in the galaxy. Although efforts were made to mitigate this effect by incorporating an α_{CO} value that accounts for photodissociation, this adjustment may still introduce a systematic bias. To study this, we obtained the molecular masses using [C II] for the arcs J1226A and J1226B. The unlensed values were $(4.9 \pm 1.1) \times 10^8 M_{\odot}$ and $(1.2 \pm 0.2) \times 10^{10} M_{\odot}$ respectively. These results will be presented in Solimano et al. (in prep.). The estimation details are found in Appendix A. In the case of J1226B, this value is lower than the upper limit obtained by CO, indicating consistency between both methods. However, for J1226B, the value is significantly higher, supporting the idea that CO may not be a good tracer of molecular gas in some cases. From what we obtained from the stacking the CO only traces 9% of the gas traced by the dust, meaning part of the galaxies' gas could be CO-dark.

Lastly, a plausible explanation for the apparent gas deficit observed in our study is that it is accurate. In this scenario, we can draw parallels with the MS SBs proposed by Gómez-Guijarro et al. (2022). While they primarily identified high-mass galaxies as MS SBs ($> \text{Log}(M_*) = 10.55$), our results suggest that low-mass galaxies could exhibit similar characteristics, namely low depletion times and low gas fractions, while remaining in the main sequence. Though our depletion times and gas fractions are larger than theirs, most are upper limits, meaning they could eventually coincide. Gómez-Guijarro et al. (2022) proposed two potential mechanisms through which galaxies could achieve these characteristics. The first scenario involves the compaction of the galaxy's core following a gas-rich merger, leading to gas funneling toward the center. This process increases the SFR, causing the galaxy to move upward in the main sequence plot. Subsequently, as the gas is consumed, the galaxy gradually lowers its SFR, traversing through the main sequence phase. The second scenario states that gas is funneled toward the galaxy's center, increasing star formation activity. As the gas supply is depleted over time, the star-forming region becomes more compact, sustaining a high SFR. Eventually, this process may result in forming a compact star-forming core, which continues to fuel star formation activity. Of the two, this second scenario is the most probable explanation for the observed characteristics in our galaxies. Unlike mergers that typically result in the formation of more giant galaxies, the sustained star formation with less gas than expected suggests a mechanism wherein gas is efficiently funneled toward the galaxy's center, enabling sustained star formation despite the gas deficit.

After considering various explanations for the observed gas deficit in the studied galaxies, we find that a combination of factors is likely at play. Due to our data, we believe the most likely scenario is a mixture of CO-dark gas and a relatively high atomic gas reservoir. From the stacked values, we obtain that CO only traced 9% of the gas by the dust emission, which could indicate that the rest of the gas is in atomic form. However, due to the low metallicity of the studied galaxies, it is paramount to consider that some of the gas might not be well traced by CO. Due to this, it is more accurate to consider the 91% of atomic gas to be an upper limit of atomic gas rather than the absolute value.

5. Summary and conclusions

This research focused on twelve gravitationally lensed low-mass SFGs with redshifts between 1.9 and 3.6. We used ACA observations to search for CO emission lines and to analyze the galaxies' dust continuum in order to estimate different molecular gas mass values. We obtained three different values, one using CO and two using dust masses at different wavelengths. Additionally, we utilized supplementary HST and JWST data for SED fitting, allowing us to obtain the intrinsic properties of the galaxies after correcting by the gravitational magnification factor.

CO was only detected in three of the twelve arcs (J0033, J0108, and J1050A). In contrast, three galaxies were detected in 870 μm /1.25mm dust continuum (J0033, J1050, J1226B), with no galaxies detected in 2.1/3.1 mm dust continuum. Additionally, we created stacked versions of our data to gain insights into the average properties of our sample.

When comparing our data with reported scaling relations (Speagle et al., 2014; Tacconi et al., 2018) we found that all the galaxies belonged in the main sequence. Some galaxies exhibit an apparent deficit of molecular gas compared with the extrapolation of scaling relations fitted to more massive galaxies at similar redshifts. To explain this deficit, we discussed four scenarios. We explored the possibilities of systematic errors associated with the molecular gas estimate and the scenario of a main sequence starburst. However, assuming our gas estimates are correct, it seems that a combination of CO-dark gas in these low-metallicity galaxies and the predominant presence of gas in the atomic phase primarily drives the low molecular gas fraction and depletion times we observe.

This assumption arises from our stacked sample, as we obtained that 91% of the gas may be in atomic form. However, we consider this an upper limit as CO-dark gas may also affect the obtained CO measurements, corroborated by the [C II] observations for J1226B. To further test this hypothesis, we must investigate the [C II] emission for the rest of the studied galaxies when allowed by their redshifts. This would tell us if we are under the presence of CO-dark gas and would allow us to determine if the 91% value obtained is an upper limit or an accurate estimate of the galaxy's atomic gas content.

References

- Accurso, G., Saintonge, A., Catinella, B., et al. 2017, *Monthly Notices of the Royal Astronomical Society*, 470, 4750
- Aravena, M., Decarli, R., González-López, J., et al. 2019, *The Astrophysical Journal*, 882, 136
- Bayliss, M. B., Rigby, J. R., Sharon, K., et al. 2014, *The Astrophysical Journal*, 790, 144
- Boquien, M., Burgarella, D., Roehly, Y., et al. 2019, *Astronomy & Astrophysics*, 622, A103
- Brisbin, D., Aravena, M., Daddi, E., et al. 2019, *Astronomy and Astrophysics*, 628, A104
- Bruzual, G. & Charlot, S. 2003, *Monthly Notices of the Royal Astronomical Society*, 344, 1000
- Carilli, C. & Walter, F. 2013, *Annual Review of Astronomy and Astrophysics*, 51, 105
- CASA Team, Bean, B., Bhatnagar, S., et al. 2022, *Publications of the Astronomical Society of the Pacific*, 134, 114501
- Casey, C. M., Zavala, J. A., Aravena, M., et al. 2019, *The Astrophysical Journal*, 887, 55
- Castillo, M. F., Hodge, J., Rybak, M., et al. 2023, *The Astrophysical Journal*, 945, 128
- Chabrier, G. 2003, *Publications of the Astronomical Society of the Pacific*, 115, 763
- Charlot, S. & Fall, S. M. 2000, *The Astrophysical Journal*, 539, 718
- Chisholm, J., Rigby, J. R., Bayliss, M., et al. 2019, *The Astrophysical Journal*, 882, 182
- Daddi, E., Dannerbauer, H., Liu, D., et al. 2015, *Astronomy & Astrophysics*, 577, A46
- Dahle, H., Aghanim, N., Guennou, L., et al. 2016, *Astronomy & Astrophysics*, 590, L4
- Dale, D. A., Helou, G., Magdis, G. E., et al. 2014, *The Astrophysical Journal*, 784, 83
- Dessauges-Zavadsky, M., Zamojski, M., Schaerer, D., et al. 2015, *Astronomy & Astrophysics*, 577, A50
- Diehl, H. T., Allam, S. S., Annis, J., et al. 2009, *The Astrophysical Journal*, 707, 686
- Fischer, T. C., Rigby, J. R., Mahler, G., et al. 2019, *The Astrophysical Journal*, 875, 102
- Genzel, R., Tacconi, L. J., Combes, F., et al. 2012, *The Astrophysical Journal*, 746, 69
- Genzel, R., Tacconi, L. J., Lutz, D., et al. 2015, *The Astrophysical Journal*, 800, 20
- Gómez-Guijarro, C., Elbaz, D., Xiao, M., et al. 2022, *Astronomy and Astrophysics*, 659, A196
- Hatsukade, B., Hashimoto, T., Kohno, K., et al. 2019, *The Astrophysical Journal*, 876, 91
- Hennawi, J. F., Gladders, M. D., Oguri, M., et al. 2008, *The Astronomical Journal*, 135, 664
- Henríquez-Brocal, K., Herrera-Camus, R., Tacconi, L., et al. 2022, *Astronomy and Astrophysics*, 657, L15
- Hughes, T. M., Ibar, E., Villanueva, V., et al. 2017, *Astronomy and Astrophysics*, 602, A49
- Jullo, E. & Kneib, J. P. 2009, *Monthly Notices of the Royal Astronomical Society*, 395, 1319
- Kaur, B., Kanekar, N., Rafelski, M., et al. 2022, *The Astrophysical Journal*, 933, L42
- Koester, B. P., Gladders, M. D., Hennawi, J. F., et al. 2010, *The Astrophysical Journal Letters*, 723, L73
- Lagos, C. d. P., Crain, R. A., Schaye, J., et al. 2015, *Monthly Notices of the Royal Astronomical Society*, 452, 3815
- Leitherer, C., Schaerer, D., Goldader, J. D., et al. 1999, *The Astrophysical Journal Supplement Series*, 123, 3
- Lenkić, L., Bolatto, A. D., Fisher, D. B., et al. 2023, *The Astrophysical Journal*, 945, 9
- Madau, P. & Dickinson, M. 2014, *Annual Review of Astronomy and Astrophysics*, 52, 415
- Madden, S. C., Cormier, D., Honig, S., et al. 2020, *Astronomy and Astrophysics*, 643, A141
- Magdis, G. E., Daddi, E., Elbaz, D., et al. 2011, *The Astrophysical Journal*, 740, L15
- Marques-Chaves, R., Pérez-Fournon, I., Shu, Y., et al. 2017a, *The Astrophysical Journal*, 834, L18
- Marques-Chaves, R., Pérez-Fournon, I., Shu, Y., et al. 2017b, *The Astrophysical Journal*, 834, L18
- Messias, H., Guerrero, A., Nagar, N., et al. 2024, *Monthly Notices of the Royal Astronomical Society*
- Motta, V., Ibar, E., Verdugo, T., et al. 2018, *The Astrophysical Journal*, 863, L16
- Narayanan, D. & Krumholz, M. 2014, *Monthly Notices of the Royal Astronomical Society*, 442, 1411
- Oguri, M., Hennawi, J. F., Gladders, M. D., et al. 2009, *The Astrophysical Journal*, 699, 1038
- Papadopoulos, P. P., van der Werf, P. P., Xilouris, E. M., et al. 2012, *Monthly Notices of the Royal Astronomical Society*, 426, 2601
- Popping, G., Somerville, R. S., & Trager, S. C. 2014, *Monthly Notices of the Royal Astronomical Society*, 442, 2398

- Ramambason, L., Leboutteiller, V., Madden, S. C., et al. 2024, *Astronomy and Astrophysics*, 681, A14
- Riechers, D. A., Bradford, C. M., Clements, D. L., et al. 2013, *Nature*, 496, 329
- Rigby, J. R., Bayliss, M., Fischer, T. C., et al. 2017, JWST Proposal ID 1355. Cycle 0 Early Release Science, 1355
- Rigby, J. R., Bayliss, M. B., Gladders, M. D., et al. 2014, *The Astrophysical Journal*, 790, 44
- Rigby, J. R., Bayliss, M. B., Sharon, K., et al. 2018, *The Astronomical Journal*, 155, 104
- Rivera-Thorsen, T. E., Dahle, H., Gronke, M., et al. 2017, *Astronomy and Astrophysics*, 608, L4
- Saintonge, A. & Catinella, B. 2022, *Annual Review of Astronomy and Astrophysics*, 60, 319
- Saintonge, A., Catinella, B., Tacconi, L. J., et al. 2017, *The Astrophysical Journal Supplement Series*, 233, 22
- Saintonge, A., Lutz, D., Genzel, R., et al. 2013, *The Astrophysical Journal*, 778, 2
- Sanders, R. L., Shapley, A. E., Jones, T., et al. 2021, *The Astrophysical Journal*, 914, 19
- Sanders, R. L., Shapley, A. E., Jones, T., et al. 2023, *The Astrophysical Journal*, 942, 24
- Schruba, A., Leroy, A. K., Walter, F., et al. 2012, *The Astronomical Journal*, 143, 138
- Scoville, N., Aussel, H., Sheth, K., et al. 2014, *The Astrophysical Journal*, 783, 84
- Scoville, N., Sheth, K., Aussel, H., et al. 2016, *The Astrophysical Journal*, 820, 83
- Sharon, K., Bayliss, M. B., Dahle, H., et al. 2020, *The Astrophysical Journal Supplement Series*, 247, 12
- Sharon, K., Cerny, C., Rigby, J. R., et al. 2022a, HST-Based Lens Model of SDSS J1226+2152, in Preparation for JWST-ERS TEMPLATES
- Sharon, K., Cerny, C., Rigby, J. R., et al. 2022b, HST-Based Lens Model of the First Extragalactic JWST Science Target, SDSS J1226+2152, in Preparation for TEMPLATES
- Sharon, K., Mahler, G., Rivera-Thorsen, T. E., et al. 2022c, *The Astrophysical Journal*, 941, 203
- Solimano, M., González-López, J., Barrientos, L. F., et al. 2021, *Astronomy & Astrophysics*, 655, A42
- Speagle, J. S., Steinhardt, C. L., Capak, P. L., & Silverman, J. D. 2014, *The Astrophysical Journal Supplement Series*, 214, 15
- Spilker, J. S., Phadke, K. A., Aravena, M., et al. 2023, *Nature*, 618, 708
- Tacconi, L. J., Genzel, R., Saintonge, A., et al. 2018, *The Astrophysical Journal*, 853, 179
- Tacconi, L. J., Genzel, R., & Sternberg, A. 2020, *Annual Review of Astronomy and Astrophysics*, 58, 157
- Taniguchi, Y. & Ohyama, Y. 1998, *The Astrophysical Journal*, 509, L89
- Tsujita, A., Kohno, K., Huang, S., et al. 2024, ALMA Lensing Cluster Survey: Physical Characterization of near-Infrared-Dark Intrinsically Faint ALMA Sources at $Z=2-4$
- Tsukui, T., Iguchi, S., Mitsuhashi, I., & Tadaki, K. 2023, *Journal of Astronomical Telescopes, Instruments, and Systems*, 9, 018001
- Vizgan, D., Heintz, K. E., Greve, T. R., et al. 2022, *The Astrophysical Journal*, 939, L1
- Wilson, C. D. 1995, *The Astrophysical Journal*, 448, L97
- Zanella, A., Daddi, E., Magdis, G., et al. 2018, *Monthly Notices of the Royal Astronomical Society*, 481, 1976

Appendix A: Gas mass from [C II] emission in SGASJ1226

As suggested by Madden et al. (2020) and others, low metallicity molecular clouds have their CO emission heavily suppressed and are photon-dominated very deep into their inner regions. For this reason, several authors argue that in these regimes, the bulk of molecular gas is better traced by fine structure [C II] emission line at a rest frequency of 1900.536 GHz (Accurso et al. (2017), Hughes et al. (2017), Zanella et al. (2018), Vizgan et al. (2022)). To test this idea, we have obtained [C II] observations of the SGASJ1226 field, covering two galaxies of our sample (ALMA program 2021.1.01337.S, PI: Solimano). A full analysis of these data will be presented in Solimano et al. (in prep.). The observations combine data from the 7m array and the 12m arrays. We reduce the visibility data using the standard pipeline version [XX], and then synthesize datacubes using the multiscale deconvolver, adopting a channel width of 9.6 km s^{-1} , and restoring with a common circular beam size of 0.72 arcseconds. We achieve a point-source sensitivity of $1\sigma = 2.4 \text{ mJy beam}^{-1} \text{ channel}^{-1}$.

We visually inspect the datacube and extract spectra from apertures that roughly match the apertures of arcs A.1 and B used for photometric extraction (see Fig. 1), but accounting for the larger beam compared to the HST and JWST imaging. The line is robustly detected in both arcs, with an integrated S/N of ~ 12 in the brightest region (within arc B). We fit Gaussians to the PB-corrected 1D spectra, with one kinematic component for arc A.1, and two for arc B. We measure total integrated fluxes of $3.3 \pm 0.5 \text{ Jy km s}^{-1}$ and $15.72 \pm 0.24 \text{ Jy km s}^{-1}$ in arcs A.1 and B, respectively. These fluxes translate into image-plane luminosities of $\mu L_{[\text{C II}]}^{\text{A.1}} = (1.0 \pm 0.14) \times 10^9 L_{\odot}$ and $\mu L_{[\text{C II}]}^{\text{B}} = (4.81 \pm 0.07) \times 10^9 L_{\odot}$.

Following Zanella et al. (2018), we adopt a [C II]-to- H_2 conversion factor of $\alpha_{[\text{C II}]} = 30 M_{\odot} L_{\odot}^{-1}$, which yields delensed molecular gas masses of $(4.9 \pm 1.1) \times 10^8 M_{\odot}$ and $(1.2 \pm 0.2) \times 10^{10} M_{\odot}$, for arcs A.1 and B, respectively. Taken at face value, the inferred mass for SGASJ1226-A is consistent with our CO and dust upper limits, and confirms a low gas fraction of 0.05 ± 0.02 . Meanwhile, the gas mass inferred for SGASJ1226-B is significantly larger than our CO-based upper limit, albeit consistent with our value derived from the dust detection ($M_{\text{mol}} = (9 \pm 2) \times 10^9 M_{\odot}$). The [C II]-derived mass implies a gas fraction as high as 1.2 ± 0.3 .

These results suggest that despite the similar masses and colors of SGASJ1226-A and SGASJ1226-B, they seem to differ significantly in their cold ISM properties. On the one hand, galaxy B harbors a larger content of dust, although not enough to shield CO molecules from photo-dissociation. On the other hand, galaxy A appears gas-deficient, although we caution that the $\alpha_{[\text{C II}]}$ factor is just as uncertain (or even more) than α_{CO} , due to its sensitivity to metallicity, density and temperature [cite]. So far, we have assumed that A and B have the same metallicity, but that might not be the case. This hypothesis will be tested with upcoming observations of this system with JWST/NIRSpec (GO-3777), as they will provide nebular strong line estimations of the metallicity of both galaxies.

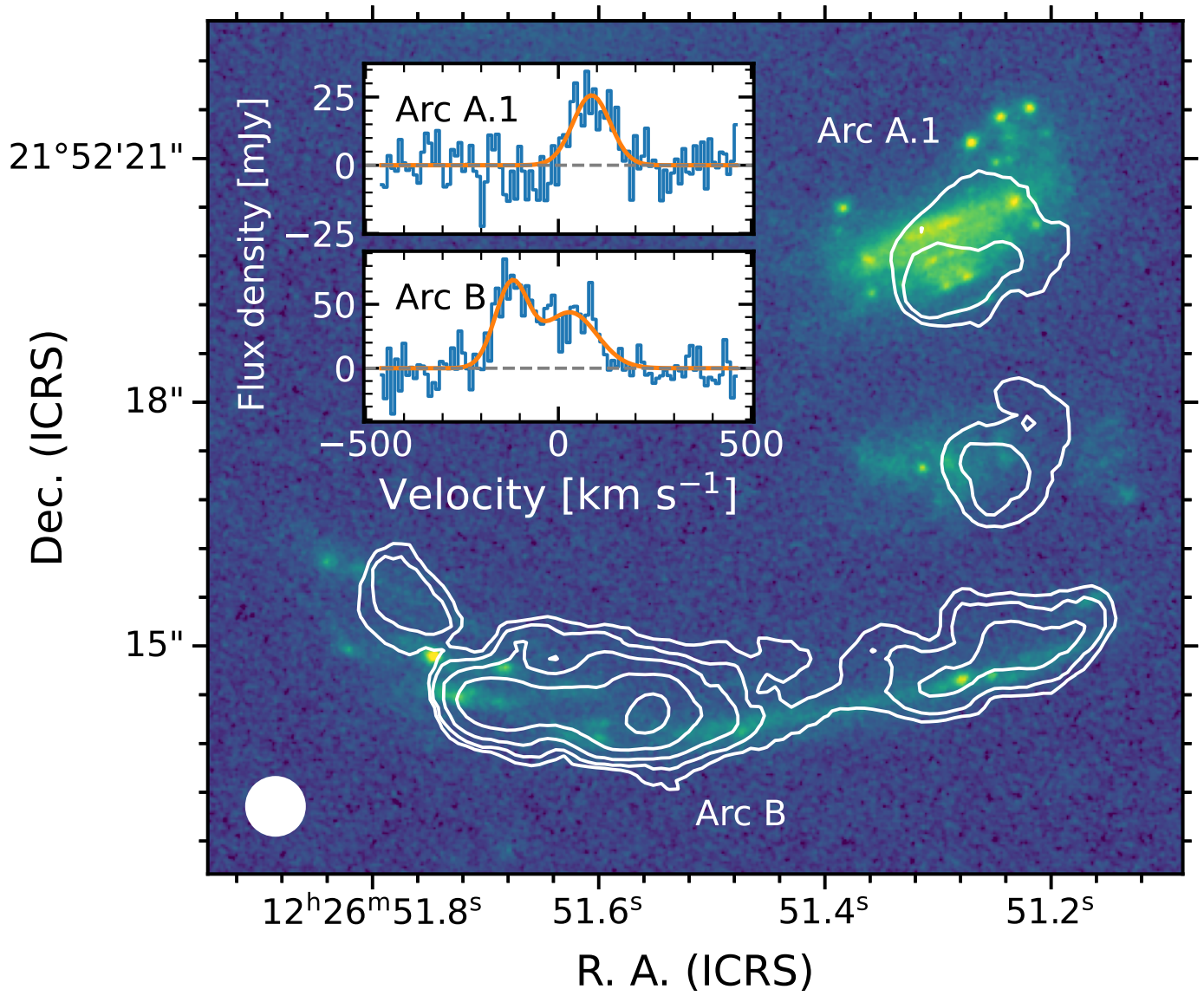
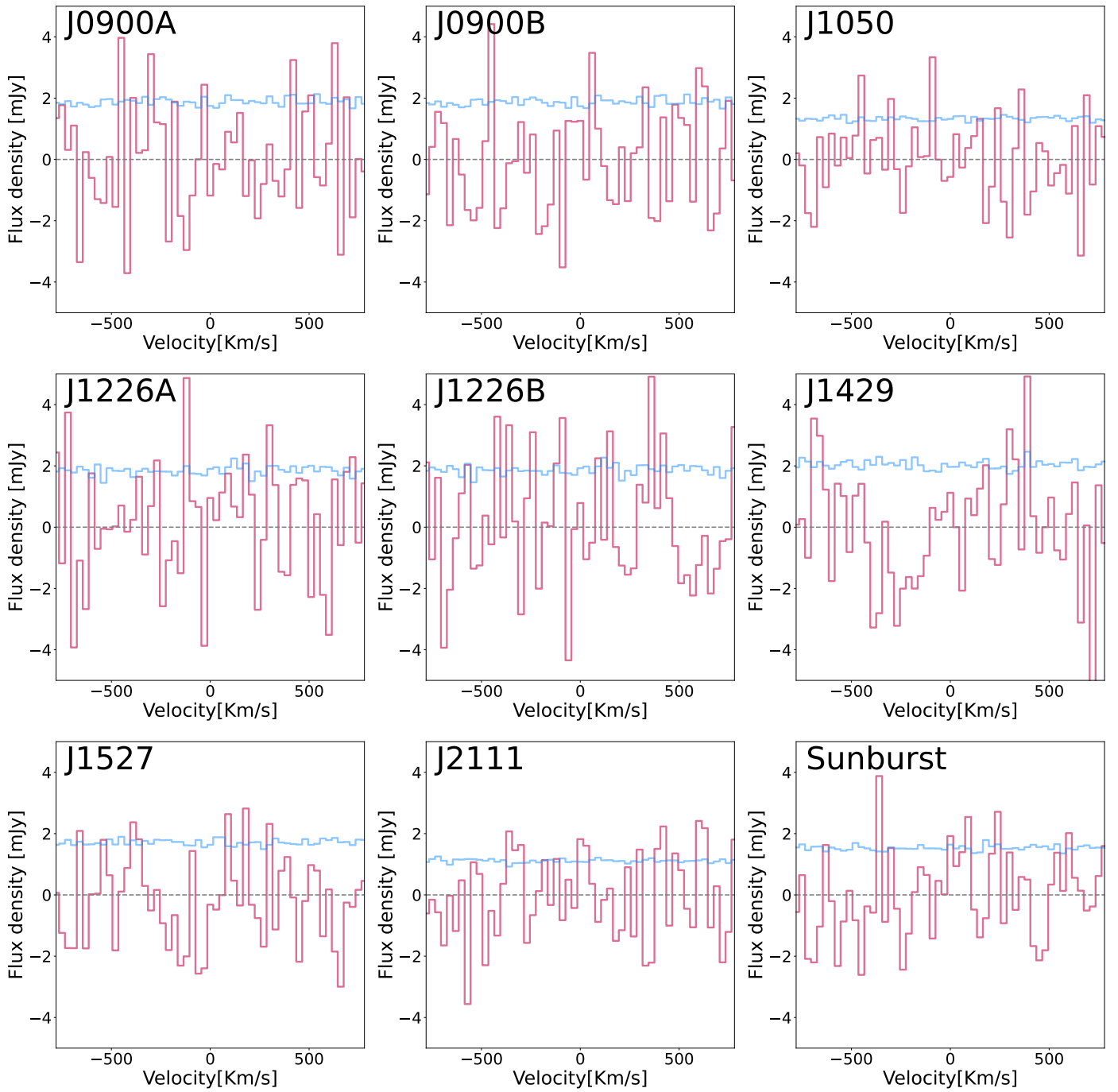


Fig. A.1: HST ACS/F606W image of the SGASJ1226 field with ALMA [C II] contours (white). The first contour is at the surface brightness level of $0.21 \text{ Jy km s}^{-1} \text{ beam}^{-1}$, which corresponds to $S/N \sim 3$. Subsequent levels increase as powers of $\sqrt{3}$. Inset axes show the integrated spectra of SGASJ1226-A.1 (top) and SGASJ1226-B (bottom).

Appendix B: Non detection spectras

Fig. B.1: Spectrum of arcs, where the pink line indicates the spectrum and the blue line a 1σ error

Appendix C: SED fits

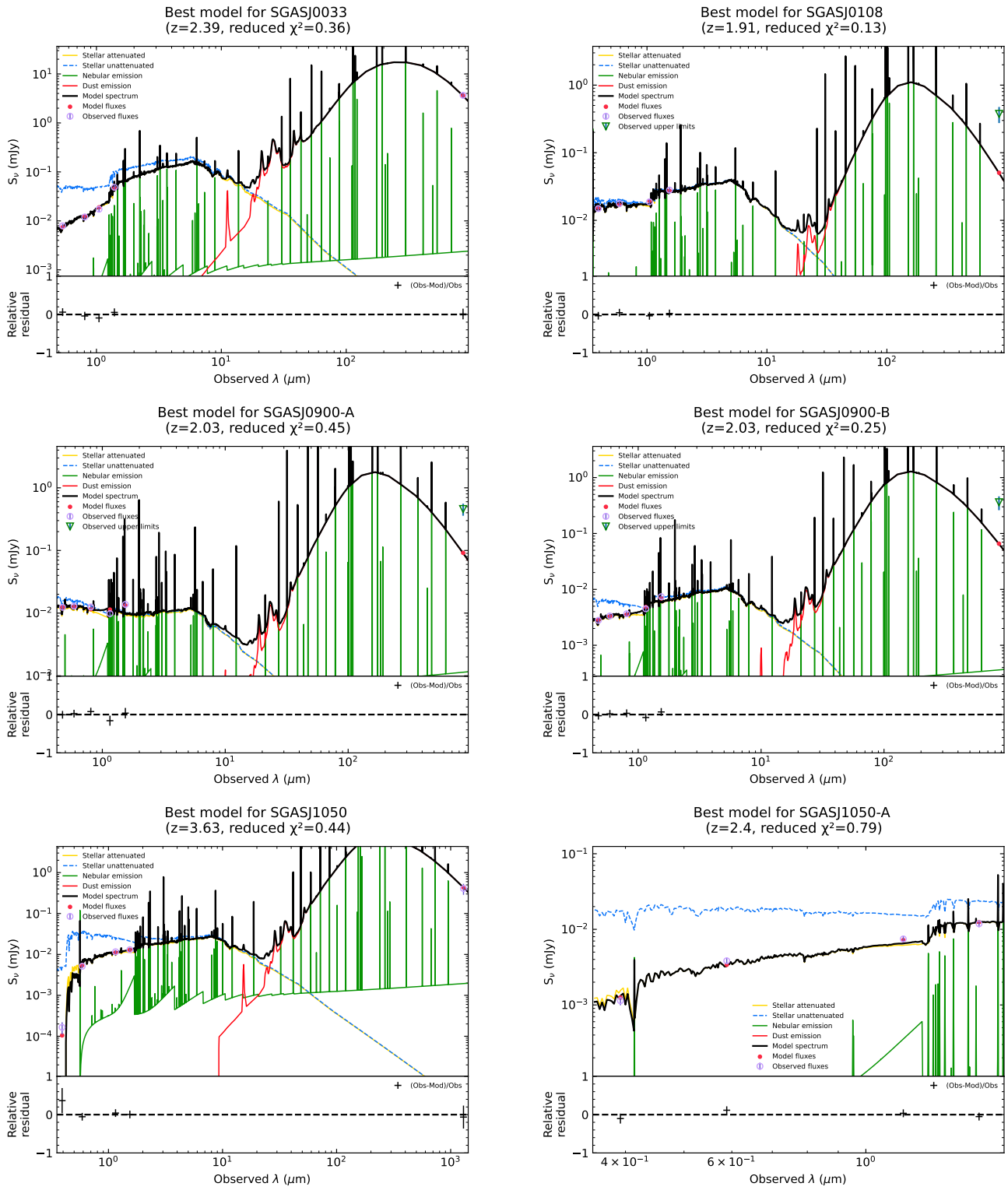


Fig. C.1: SED fit for the gravitational arcs using HST and ALMA photometry, modeled with CIGALE to derive the physical properties.

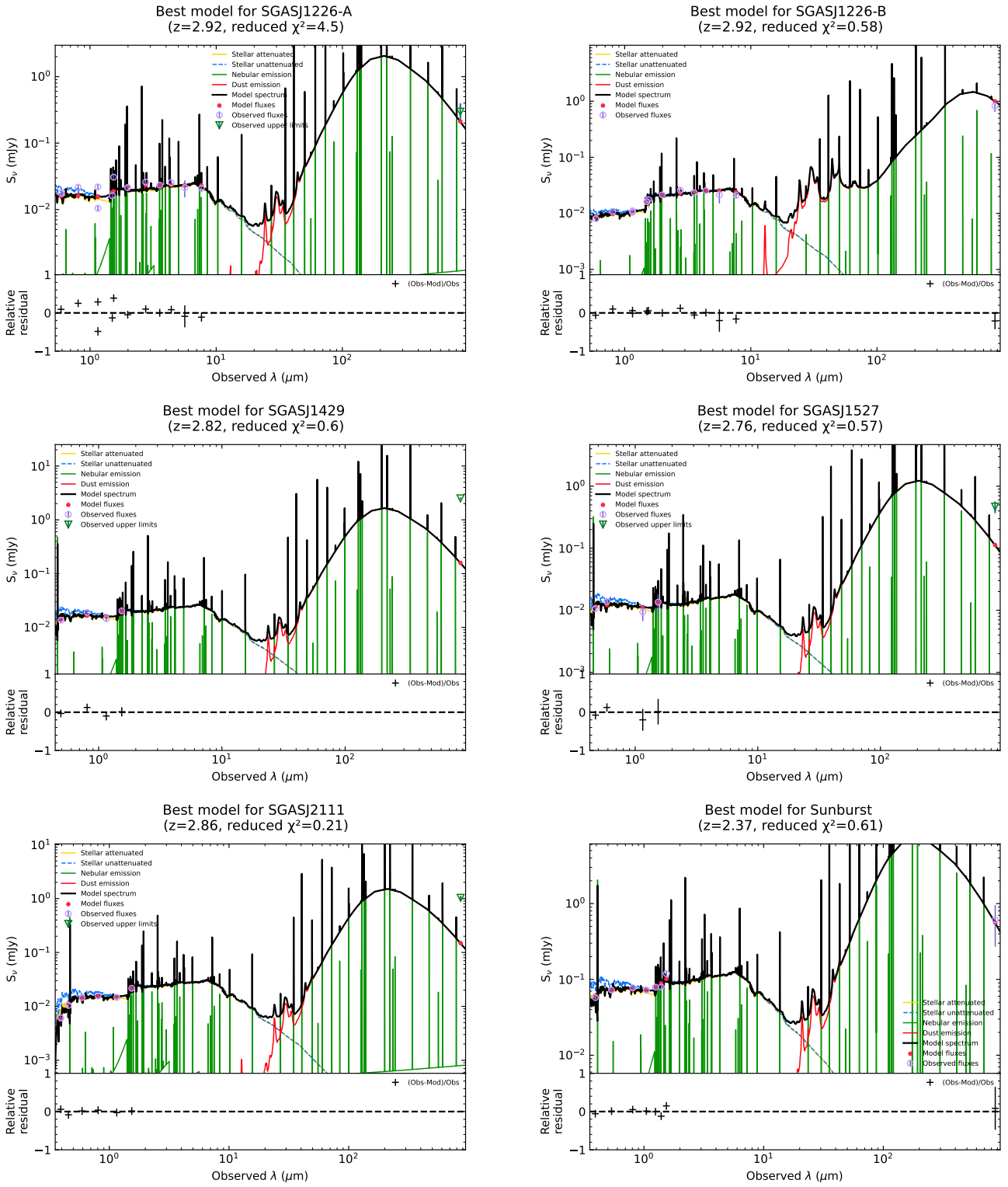


Fig. C.2: Continuation of Fig. C.1

Appendix D: Data for R_{j1}

Table D.1: The dataset utilized for developing models linking ΣSFR and R_{j1}

Galaxy	z	Σ_{SFR} [$M_{\odot}\text{yr}^{-1}\text{kpc}^{-2}$]	R_{31}	R_{41}	R_{51}	Reference
D13-5	0.075	0.066	0.55±0.02	0.32±0.01	-	1
D15-3	0.067	0.024	-	0.16±0.01	-	1
G04-1	0.130	0.02	0.54±0.04	0.28±0.02	-	1
G08-5	0.140	0.02	0.8 ±0.1	-	-	1
G14-1	0.132	0.02	0.48±0.08	0.27±0.03	-	1
G20-2	0.141	0.04	0.58±0.07	0.33±0.04	-	1
AS2COS0023.1	4.341	161.96±28.00	-	1.26±0.56	-	2
AS2UDS011.0*	4.073	587.80±251.10	-	1.46±0.93	-	2
AS2UDS026.0	3.296	73.71±31.50	-	1.22±0.51	-	2
CDFN8	4.144	117.10±41.00	-	1.07±0.38	-	2
AS2COS0031.1	3.643	27.28±9.30	-	0.51±0.15	-	2
AS2COS0054.1	3.174	130.00±32.80	-	0.42±0.18	-	2
AS2COS0008.1	3.581	161.00±28.90	-	0.63±0.22	-	2
CDFN2	4.422	252.20±67.50	-	0.59±0.18	-	2
AS2UDS012.0	2.520	46.70±8.30	0.37±0.11	-	-	2
AS2UDS010.0	3.169	99.10±30.90	0.6±0.18	-	-	2
AS2COS0013.1	2.608	95.40±21.60	1.16±0.24	-	-	2
CDFN1	3.159	168.80±46.20	0.31±0.09	-	-	2
AS2UDS126.0	2.436	467.10±382.90	0.9±0.56	-	-	2
HOSTGALAXY GRB080207	2.086	3.40	1.098±1.09	0.988±1.02	-	3
arp 220	0.018	411.10	0.97±0.14	-	-	4,5
NGC 6240	0.024	4.94	1.1±0.24	-	-	4,5
NGC 7469	0.016	11.32	0.6±0.1	0.83±0.19	-	4,5
Zw 049.057	0.013	22.59	0.66±0.11	0.58±0.15	-	4,5
arp 193	0.023	149.26	0.74±0.12	-	-	4,5
NGC 1068	0.004	210.84	0.67±0.16	-	-	4,5
B1228-113	2.193	1.79	0.86±0.21	-	-	6
j0918+1636	2.585	6.21	1.0±0.2	1.03±0.23	0.39	6
BzK-4171	1.465	0.80	0.47±0.15	-	0.37	7
BzK-16000	1.525	0.82	0.27±0.07	-	0.12	7
BzK-21000	1.521	1.68	0.57±0.14	-	0.36	7
HFLS3	6.340	600.00	1.08±0.17	-	-	8
BX610	2.200	1.61	0.92±0.17	1.08±0.22	-	9
MD94	2.000	1.89	1.21±0.13	-	-	10

References. (1) Lenkić et al. (2023),(2) Castillo et al. (2023),(3) Hatsukade et al. (2019),(4) Taniguchi & Ohyama (1998),(5) Papadopoulos et al. (2012),(6) Kaur et al. (2022),(7) Daddi et al. (2015),(8) Riechers et al. (2013),(9) Brisbin et al. (2019) ,(10) Henríquez-Brocal et al. (2022)

Appendix E: Cigale Parameters

This section outlines the parameters employed in running CIGALE. Constant parameters are detailed in Table E.1, while variable parameters are listed in Table E.2.

Table E.1: CIGALE parameters that remained constant across all arcs.

Module	Parameter	Values
bc03	imf	0
	metallicity	0.02
	separation_age	10
dustatt_modified_CF00	Av_ISM	"eval np.arange(0,2,0.05)"
	mu	0.44
	slope_ISM	-0.7
	slope_BC	-1.3
	filters	V_B90,FUV
nebular	logU	-2.0
	zgas	0.02
	ne	100
	f_esc	0.0
	lines_width	300
	emission	True
dale2014	fracAGN	0
	alpha	0.0625,0.5000,1.0000, 1.5000, 2.0000 2.5000, 3.0000, 3.5000, 4.0000
sfhdelayed	sfr_A	1.0
	normalize	True
	tau_main	2000
	f_burst	0, 0.01, 0.05, 0.1,0.25
restframe_parameters	beta_calz94	True
	D4000	False
	IRX	False
	luminosity_filters	FUV, V_B90
	colours_filters	FUV-NUV, NUV-r_prime

Table E.2: Variations in CIGALE parameters utilized for each arc.

Arc	Module	Parameter	Values
0033	sfhdelayed	age_main	1000,1500,2000,2500
		tau_burst	10, 25, 50, 100, 250, 500
		age_burst	25, 50, 100, 250,500,1000
0108	sfhdelayed	age_main	500,1000,2000,2200
		tau_burst	10, 25, 50, 100, 250, 500
		age_burst	25, 50, 100, 250,500
0900	sfhdelayed	age_main	500, 1000, 1500, 2000, 2500,3000
		tau_burst	10, 25, 50, 100, 250, 500
		age_burst	25, 50, 100, 250,500
1050	sfhdelayed	age_main	500,1000,1500
		tau_burst	10, 25, 50, 100, 250
		age_burst	25, 50, 100, 250,500
1050A	sfhdelayed	age_main	500,1000,1500,2000,2500
		tau_burst	10, 25, 50, 100, 250, 500
		age_burst	25, 50, 100, 250,500
1226	sfhdelayed	age_main	200,500,1000,1200, 1800
		tau_burst	10, 25, 50, 100, 250, 500, 1000
		age_burst	25, 50, 100
1429	sfhdelayed	age_main	100,500,1000,1750,2080
		tau_burst	10, 25, 50, 100, 250, 500
		age_burst	25, 50, 100
1527	sfhdelayed	age_main	100,500,1000,1750,2000, 2300
		tau_burst	10, 25, 50, 100, 250, 500
		age_burst	25, 50, 100
2111	sfhdelayed	age_main	100,500,1000,1750,2050
		tau_burst	10, 25, 50, 100, 250, 500
		age_burst	25, 50, 100
Sunburst	sfhdelayed	age_main	1000,1500,2000,2500
		tau_burst	10, 25, 50, 100, 250, 500
		age_burst	25, 50, 100, 250,500,1000

Appendix F: Flux percentages

Table F.1: Percentage of total flux covered in HST apertures

Arc	Percentage
J0033	97%
J0108	99%
J0900A	95%
J0900B	94%
J1050	91%
J1050-A	91%
J1226A	90%
J1226B	90%
J1429	93%
J1527	93%
J2111	96%
Sunburst	92%